

UNCLASSIFIED

SL 80 168/P/P  
copy 1

AO 2646

Laser  
P/P, BC, M

7P  
→ L

RADC-TR-75-295  
In-house Technical Report  
January 1976



## AMOS SEEING QUALITY MEASUREMENTS

### CONTRIBUTORS

Darryl P. Greenwood	RADC	Jim Newman	AFCRL
Donald O. Tarazano	RADC	Paul F. Kellen	AERL
Duane A. Haugen	AFCRL	Merlin G. Miller	AERL
J. Chandran Kaimal	AFCRL		

Sponsored by  
Defense Advanced Research Projects Agency  
ARPA Order No. 2646

Approved for public release;  
distribution unlimited.

The views and conclusions contained in this document are those of the authors and should not be interpreted as necessarily representing the official policies, either expressed or implied, of the Defense Advanced Research Projects Agency or the U. S. Government.

Rome Air Development Center  
Air Force Systems Command  
Griffiss Air Force Base, New York 13441

PLEASE RETURN TO:

DEFENSE TECHNICAL INFORMATION CENTER  
BALLISTIC MISSILE DEFENSE ORGANIZATION  
7100 DEFENSE PENTAGON  
WASHINGTON D.C. 20301-7100

43932

UNCLASSIFIED

This report has been reviewed by the RADC Information Office (OI) and is releasable to the National Technical Information Service (NTIS). At NTIS it will be releasable to the general public including foreign nations.

This report has been reviewed and is approved for publication.

APPROVED:



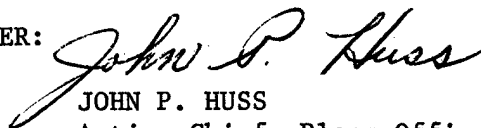
VINCENT J. COYNE  
Chief, Space Surveillance  
and Instrumentation Branch  
Surveillance Division

APPROVED:



RUDOLF C. PALTAUF  
Lt Col, USAF  
Chief, Surveillance Division

FOR THE COMMANDER:



JOHN P. HUSS  
Acting Chief, Plans Office

Do not return this copy. Retain or destroy.

Accession Number: 3932

Publication Date: Jan 01, 1976

Title: AMOS Seeing Quality Measurements

Personal Author: Greenwood, D.P.; Tarazano, D.O.; Haugen, D.A.; et al.

Corporate Author Or Publisher: Rome Air Development Center (OCSE), Griffis AFB, NY 13441 Report Number: RADC-TR-75-295 Report Number Assigned by Contract Monitor: SLL 81 168

Comments on Document: Archive, RRI, DEW

Descriptors, Keywords: AMOS Seeing Quality Measurement Atmosphere Turbulence Propagation Observatory Acoustic Sounder Maui Optical Station Astronomy Microthermal Probe TEAL BLUE Degradation Image

Pages: 00070

Cataloged Date: Nov 27, 1992

Document Type: HC

Number of Copies In Library: 000001

Record ID: 25302

Source of Document: DEW

UNCLASSIFIED

SECURITY CLASSIFICATION OF THIS PAGE (When Data Entered)

REPORT DOCUMENTATION PAGE		READ INSTRUCTIONS BEFORE COMPLETING FORM
1. REPORT NUMBER RADC-TR-75-295	2. GOVT ACCESSION NO.	3. RECIPIENT'S CATALOG NUMBER
4. TITLE (and Subtitle) AMOS SEEING QUALITY MEASUREMENTS		5. TYPE OF REPORT & PERIOD COVERED In-House Technical Report
		6. PERFORMING ORG. REPORT NUMBER ARPA Order Number 2646
7. AUTHOR(s) Darryl P. Greenwood RADC Jim Newman AFCRL Donald O. Tarazano RADC Paul F. Kellen AERL Duane A. Haugen AFCRL Merlin G. Miller AERL J. Chandran Kaimal AFCRL		8. CONTRACT OR GRANT NUMBER(s) N/A
9. PERFORMING ORGANIZATION NAME AND ADDRESS Rome Air Development Center (OCSE) Griffiss AFB NY 13441		10. PROGRAM ELEMENT, PROJECT, TASK AREA & WORK UNIT NUMBERS Program Code Number 5E20 Program Element 62301E Job Order No. 26460117
11. CONTROLLING OFFICE NAME AND ADDRESS Defense Advanced Research Projects Agency 1400 Wilson Blvd Arlington VA 22209		12. REPORT DATE January 1976
14. MONITORING AGENCY NAME & ADDRESS (if different from Controlling Office) Rome Air Development Center (OCSE) Griffiss AFB NY 13441		13. NUMBER OF PAGES 70
		15. SECURITY CLASS. (of this report) UNCLASSIFIED
		15a. DECLASSIFICATION/DOWNGRADING SCHEDULE N/A
16. DISTRIBUTION STATEMENT (of this Report)  Approved for public release; distribution unlimited.		
17. DISTRIBUTION STATEMENT (of the abstract entered in Block 20, if different from Report)  Same		
18. SUPPLEMENTARY NOTES Address for AFCRL: Address for AERL: AFCRL (LYB) AVCO Everett Research Laboratory Hanscom AFB MA 01731 2385 Revere Beach Parkway Everett MA 02149		
19. KEY WORDS (Continue on reverse side if necessary and identify by block number) Atmospheric Turbulence Observatories Propagation Acoustic Sounder Seeing Quality		
20. ABSTRACT (Continue on reverse side if necessary and identify by block number) During the month of August 1974, a series of experiments was conducted at the ARPA Maui Optical Station (AMOS) on Mt. Haleakala, Maui, Hawaii. The objectives were to quantify astronomical seeing conditions, and to determine if the seeing quality has been degraded by the presence of the site structures. Instruments used were an acoustic sounder (to probe the altitudes of 100 to 1000 ft), fine-wire microthermal probes (to measure local turbulence in and around the domes) and a Hartmann sensor (to provide integrated strengths of turbulence for the		

DD FORM 1 JAN 73 1473

EDITION OF 1 NOV 65 IS OBSOLETE

UNCLASSIFIED

SECURITY CLASSIFICATION OF THIS PAGE (When Data Entered)

19980513 280

BMC CONSULTING 4

UNCLASSIFIED

SECURITY CLASSIFICATION OF THIS PAGE(When Data Entered)

entire atmosphere). According to fine-wire probe data, local turbulence can be on occasion a significant factor in degrading seeing. These sensors noted some thermal contamination from one of the domes which was in a nearly operational configuration. The acoustic sounder indicated that the strengths of turbulence in 100 to 1000 ft altitude are not sufficient to degrade seeing. Finally, the Hartmann device recorded significantly more degradation than was seen by either of the other two probes. Hence we speculate that there is significant turbulence at high altitude temperature inversions such as at the tropopause.

UNCLASSIFIED

SECURITY CLASSIFICATION OF THIS PAGE(When Data Entered)

## PREFACE

A major part of ARPA's Advanced Optics Program under TEAL BLUE II is the characterization of seeing at the ARPA Maui Optical Station (AMOS). The site is located atop Mt. Haleakala, about 10,000 ft above sea level, on the island of Maui, Hawaii. Presumably this is an environment where degradation of optical imaging due to turbulent fluctuations in the index of refraction is minimal. The experiment described herein is the first in a group of diverse projects which will define the limitations of this site. In the experiment of August 1974, optical, micro-meteorological and acoustic instruments were used to probe the turbulence structure.

The work of AVCO Everett Research Lab was in the optical area, using a Hartmann device, and was supported by contract F30602-75-C-0012 with RADC. The Boundary Layer Branch at AFCRL had the responsibility for recording and processing the meteorological and sounder data. The RADC Environmental Studies Section was the coordinating agency and had the responsibility during the experiment for the microthermal probes. The report itself, while compiled and edited at RADC, may be considered as coming from equal contributions of the three agencies.

## ACKNOWLEDGMENTS

We thank all of the Lockheed and AVCO employees at AMOS who were particularly helpful to us during our experiments. Mr. Paul Zieske, AVCO, and Mr. Thomas Reed, Lockheed, in particular, provided us with invaluable assistance and advice during all phases of the program.

# TABLE OF CONTENTS

	Page
PREFACE .....	i
ACKNOWLEDGEMENTS.....	ii
I. INTRODUCTION.....	1
A. Background.....	1
B. Experimental Plan.....	4
C. General Conclusions.....	5
II. TURBULENCE MEASUREMENTS.....	7
A. Experimental Design.....	7
B. Data Analysis Procedures for the Fine-Wire Probes.....	9
C. Conversion of Standard Deviation to $C_T^2$ .....	11
D. Discussion of the Qualitative Nature of the Data.....	16
E. Quantization in Terms of Seeing Degradation.....	33
III. ACOUSTIC SOUNDER CALIBRATED DATA.....	39
A. Background.....	39
B. Calibration Set-up.....	39
C. Brief Remarks on Theory of Operation.....	40
D. Results of Calibration at Nevada.....	40
E. Description of AMOS Data.....	42



## TABLE OF CONTENTS (continued)

	Page
IV. OPTICAL MEASUREMENTS.....	46
A. Experimental Technique.....	46
B. Instrument.....	47
C. Measurements.....	49
D. Data Processing.....	52
E. Results.....	55
V. CONCLUSIONS.....	60
A. Comparison of All the Data.....	60
B. Summary of Conclusions.....	63
C. Recommendations and Future Work.....	64
APPENDIX A.....	66
REFERENCES.....	70

# LIST OF FIGURES

	Page
1. Aerial view of the summit of Mt. Haleakala, taken roughly to the ENE, looking into crater...	2
2. Aerial view of AMOS, showing location of sensors used in this experiment.....	3
3. Power spectra for Run 16 for microthermal sensors 1, 4 and 5.....	13
4. Outer scale $L_0$ versus time from start of mission for Runs 7, 13 and 15, on three different nights.....	15
5-18. Plots of $C_T^2$ and acoustic sounder returns versus time during the mission.....	17-31
19. Profiles of turbulence for Runs 10-13 and 15-18 as sensed by the acoustic sounder.....	44
20. Schematic diagram of Optical System.....	48
21. Measured Differential Angle of Arrival Standard Deviations and Derived Values of $r_0$ .....	58

# LIST OF TABLES

	Page
1. Position of microthermal sensors for August 1974 AMOS experiments.....	8
2. Summary of August 1974 AMOS experiments.....	12
3. Values of $r_0$ (m) for microthermal probes assuming the extent of the turbulence L is 10 m.....	36-37
4. Values of integrated $C_n^2$ and coherence length $r_c$ for the acoustic sounder profiles.....	45
5. Optical data summary.....	50-51
6. Sample data reduction.....	53
7. Differential angle of arrival measurements.....	56
8. Comparison of values of $r_0$ (m) and percent contribution to the total $r_0$ for all instruments when all instruments were operating simultaneously .....	61

## I. INTRODUCTION

### A. Background.

The Strategic Technology Office of the Defense Advanced Research Projects Agency (ARPA) is presently pursuing an advanced technology program aimed at developing techniques for obtaining high resolution images of space objects. The prime goal is the development of a compensated imaging system which will sense the effect atmospheric turbulence has on images and correct for the phase aberrations in realtime. For the proper design of such a system, ARPA needed an objective quantification of seeing quality at their prime optical site AMOS (ARPA Maui Optical Station, located in Maui, Hawaii). An equally important goal was to determine if the seeing quality had been degraded by the presence of the site structures and therefore if it could be improved by certain modifications.

The AMOS facility, shown in the photographs of Figs. 1 and 2, is comprised of two main observation domes, one containing twin 48 inch telescopes and the other a 60 inch telescope. A third dome shown in the figure was not present during the experiments which we will describe.

The basis for the concern that seeing quality may have been reduced by the presence of the buildings is a series of measurements taken during the initial site survey.<sup>1</sup> The measurements indicated that seeing was often better than 0.4 arc sec



Figure 1. Aerial View of the Summit of Mt. Haleakala, taken roughly to the ENE, looking into crater. AMOS is at the left in this photograph.

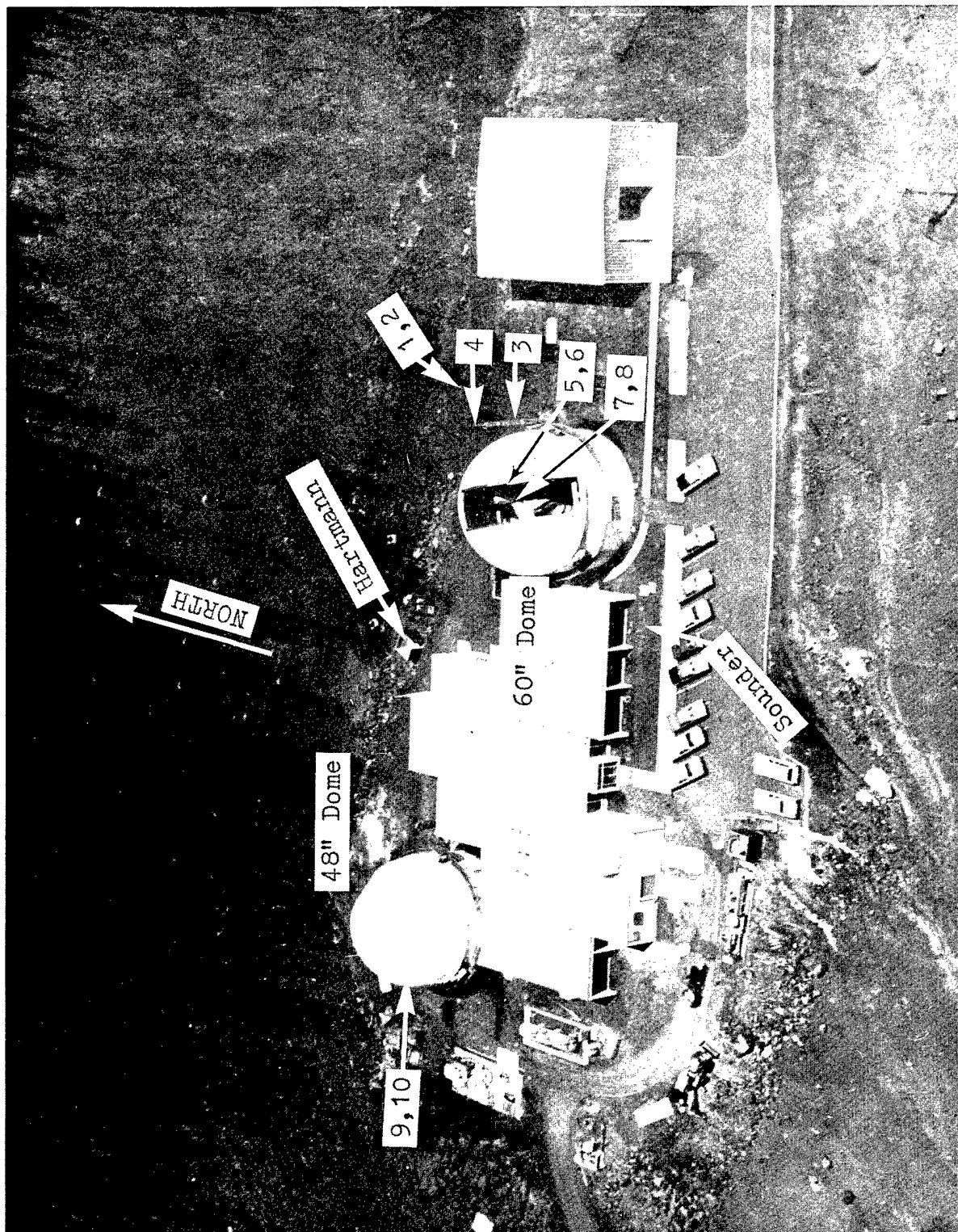


Figure 2. Aerial View of AMOS, showing location of sensors used in this experiment. Note the Acoustic Sounder and Hartmann devices are not present in this photograph.

and actually approached 0.1 arc sec at times. The confusing factor is that the telescope used was 12.5 inches in diameter. Thus the values should not be less than the Rayleigh resolution limit,  $1.22 \lambda/D$  (where  $\lambda$  = wavelength and  $D$  = diameter) which is 0.4 arc sec. Scientists using the observatory have stated that a subjective seeing limit which they observe is approximately 1 arc sec. We may either conclude there were errors in the original survey or that the dome structures did degrade the seeing.

#### B. Experimental Plan.

To pursue the objective of quantifying seeing at AMOS, the Environmental Studies Section of the Rome Air Development Center formed an experimental team consisting of their own personnel as well as those of the Boundary Layer Branch of Air Force Cambridge Research Lab (AFCRL) and AVCO Everett Research Lab (AERL). The three organizations collaborated on the formulation of the experimental plan, as well as the content of this report. The plan called for measurements of local turbulence with an acoustic sounder and fast-response microthermal probes. To determine the percentage contribution of the local effects, a measure of integrated turbulence for the whole atmosphere was to be measured with a Hartmann sensor. Data were to be taken both inside and outside the domes to determine the influence of the dome structures. Only the acoustic sounder was to operate at a fixed location, and it would provide turbulence profiles in

the altitudes of 100 to 1000 ft.

The series of experiments were run at AMOS during August 1974. RADC provided the acoustic sounder and microthermal probes and personnel to operate the microthermal devices. AFCRL provided data recording equipment, a Lyman-alpha humidimeter and a wind set, but most importantly provided scientific guidance for the experiments. AFCRL also operated the sounder as a prelude to their full calibration experiments to be undertaken just two months later. Personnel from AERL assembled the optical sensor and were responsible for its operation.

### C. General Conclusions.

Rather than to keep the reader in suspense, we will briefly summarize our most important conclusions:

(1) Although scientifically interesting activity was noted by the sounder in the range of 100-1000 ft, it was not of sufficient strength to degrade seeing.

(2) Turbulence in and around the dome structures can on occasion be a significant factor in degrading seeing.

(3) Local turbulence appears to be naturally generated in most instances, but the data are too limited to be certain. (Hence on this basis we still can not say if the original site survey data were faulty.)

(4) Additional seeing degradation is caused by thermal



contamination within the 48 inch dome.

(5) The remaining turbulence not sensed by the sounder and fine wire probes, yet sensed by the Hartmann device, must be above 1000 ft or in the range of 60 to 100 ft. Thus tropopause turbulence is probably significant.

## II. TURBULENCE MEASUREMENTS

### A. Experimental Design.

Sharp gradients in refractive index of air cause refraction and scattering of light rays. Spatial and temporal variations in these gradients are responsible generally for limitations in seeing quality, or resolution, with any given telescope. Fluctuations in the refractive index, in turn, are strongly dependent on temperature fluctuations and, to a lesser degree, on moisture fluctuations. Primary emphasis in these experiments was therefore on measuring temperature fluctuations. Up to ten microthermal sensors especially designed for measuring small scale temperature fluctuations<sup>4,5</sup> were deployed at various positions in and around the dome. The actual positions of these sensors are listed in Table 1 and depicted in the photograph of Fig. 2. In addition to these sensors, an acoustic sounder measuring echoes from temperature discontinuities up to a height of 1000 feet was used. The sounder was specially procured from the Wave Propagation Laboratory, NOAA, by RADC for use in studies of this type. Details of the acoustic sounder as an instrument for probing temperature structure may be found in a recent WPL report.<sup>6</sup> It is suffice to note here that the sounder was operated in a mode to provide usable data between heights of roughly 100 and 1000 feet.

Wind speed and direction were measured with a cup

TABLE 1

Position of Microthermal Sensors for August 1974 AMOS Experiments

<u>Position No.</u>	<u>Location</u>
1, 2	4 m above ground, 12 m NNE of 60" dome foundation, probes 1 (left) and 2 (right), separated by 0.76 m.
3	8.4 m above ground, 3 m NE of 60" dome foundation.
4	15.6 m above ground, 3 m NE of 60" dome foundation.
5	Approximately 1.5 m inside 60" dome surface, 8 m above dome floor.
6	Approximately 1.5 m outside 60" dome surface, 8 m above dome floor.
7	Inside 60" telescope tube, at base of tube.
8	Inside 60" telescope tube, at top of tube.
9	Approximately 1.5 m inside 48" dome surface, 8 m above dome floor.
10	Approximately 1.5 m outside 48" dome surface, 8 m above dome floor.

---

anemometer and a wind vane to permit relating speed and direction to the orientation of the dome slot. Moisture fluctuations were also measured with a Lyman-alpha humidimeter for a few runs to obtain preliminary data on their importance to refractive index fluctuations at AMOS. No processing of the microhumidity data was done, as it was obvious from observing the signal levels that there was insignificant humidity turbulence.

All the data were recorded on a 14-channel analog tape recorder for subsequent analysis. In addition, the acoustic sounder return was recorded on a facsimile chart as a function of time and height to provide an immediate graphic record of the spatial and temporal variations in the temperature structure. It should be noted, however, that the facsimile records provide only a qualitative measure of the echo intensity, and the variations in it, since the gain setting for the recorder is always adjusted for optimum contrast and not set at a predetermined level. The sounder data recorded on analog tape were processed at a later time to provide profiles of turbulence with accuracy of typically  $\pm 20\%$ .

#### B. Data Analysis Procedures for the Fine-Wire Probes.

The temperature data have been digitized at a rate of 10 per second for the length of each observational period, which was normally slightly in excess of three hours. The standard deviation  $\sigma_T$  of the temperature fluctuations was then computed for successive five minute periods. In addition  $C_T^2$ , the

temperature structure parameter, is computed from microtemperature measured on a pair of probes positioned away from the domes. We then calculate  $C_T^2$  for the remaining sensors for which we have only standard deviations computed. This step is imperative since it is  $C_T^2$  and *not*  $\sigma_T$  which is used in optical propagation calculations.

By definition,  $C_T^2$  is the constant of proportionality in the Kolmogorov inertial subrange form of the temperature structure function:

$$D_T(r) = C_T^2 r^{2/3}, \quad (1)$$

where  $r$  = separation (traditionally in meters). Since the structure function is the mean square value of the temperature difference for two probes separated a distance  $r$ , we may write this simple relation for  $C_T^2$ :

$$C_T^2 = \langle (T_1 - T_2)^2 \rangle r^{-2/3}, \quad (2)$$

where  $T_1$  and  $T_2$  are temperatures at positions 1 and 2, and the units of  $C_T^2$  are  $^{\circ}\text{C}^2\text{m}^{-2/3}$ . We may take the brackets  $\langle \cdot \rangle$  as representing a time average although strictly speaking they represent an ensemble average. (Hence ergodicity is assumed.)

It is reasonable to expect that the levels of turbulence inside the dome and inside the telescope tube are strongly influenced by wind speed and its direction relative to the orientation of the dome slot. That is, a large amount of turbulent

activity inside the dome can be related to turbulence in the atmosphere outside the dome, as well to thermal activity generated inside the dome. Therefore, the average wind speed and direction were computed and tabulated for each run.

Nearly all the observational periods were scheduled between local sunset and sunrise. One three-hour period was scheduled during daytime hours to obtain data during convective mixing situations for comparison purposes. A summary of the data runs completed is given in Table 2. The microtemperature sensor positions which were active for each run are listed here. This table also contains the overall mean wind speed, wind direction, and the dome slot orientation for each run.

#### C. Conversion of Standard Deviations to $C_T^2$ .

In order to use existing propagation theory, we must insure that the turbulence was Kolmogorov. Figure 3 is a set of sample spectra for Run 16 and covers an 88 minute period. Although this time period is short with respect to the entire experiment and although only three sensors are shown, we have found this to be representative of all the data. Note that the spectra exhibit a nearly  $f^{-5/3}$  behavior in the inertial subrange. Hence the turbulence appears Kolmogorov. Also note that the spectra do not flatten into an  $f^0$  power law until very low frequencies. This indicates large values of outer scale, which would be expected at these altitudes.

TABLE 2

Summary of August 1974 AMOS experiments

Run No.	Time (HST)	Day	Active Sensor Positions	Wind Speed (m/sec)	Wind Direction	Dome Slot Orientation
3	1835-2145	20	1 thru 4	2	NNW	Not opened
4	1845-2152	21	1 thru 8	4	SE	NE
5	2207-0119	21/22	1 thru 8	7	S	NE
6	0140-0450	22	1 thru 8	7	S	NE
7	1857-2205	22	1 thru 8	3	S	NE
8	2237-0145	22/23	1 thru 8	2	S	NE
9	1913-2022	23	1 thru 8	9	NNE	SW
10	2055-0006	23/24	1 thru 8	2	NNW	
11	0042-0353	24	1 thru 8	missing	NNW	SSW
12	0412-0719	24	1 thru 8	missing	NNW	SSW
13	2110-0020	24/25	1 thru 10	missing	NNE	SSW*
14	0550-0905	25	1 thru 10	4	NNE	NE*
15	2020-2325	25	1 thru 10	6	S	NE*
16	2345-0250	25/26	1 thru 10	6	S	NE*
17	1856-2002	26	1 thru 8	2	S	NE
18	2210-2328	26	1 thru 8	1	S	NE

\*The 48" dome slot, instrumented for these four runs, was oriented SSW.

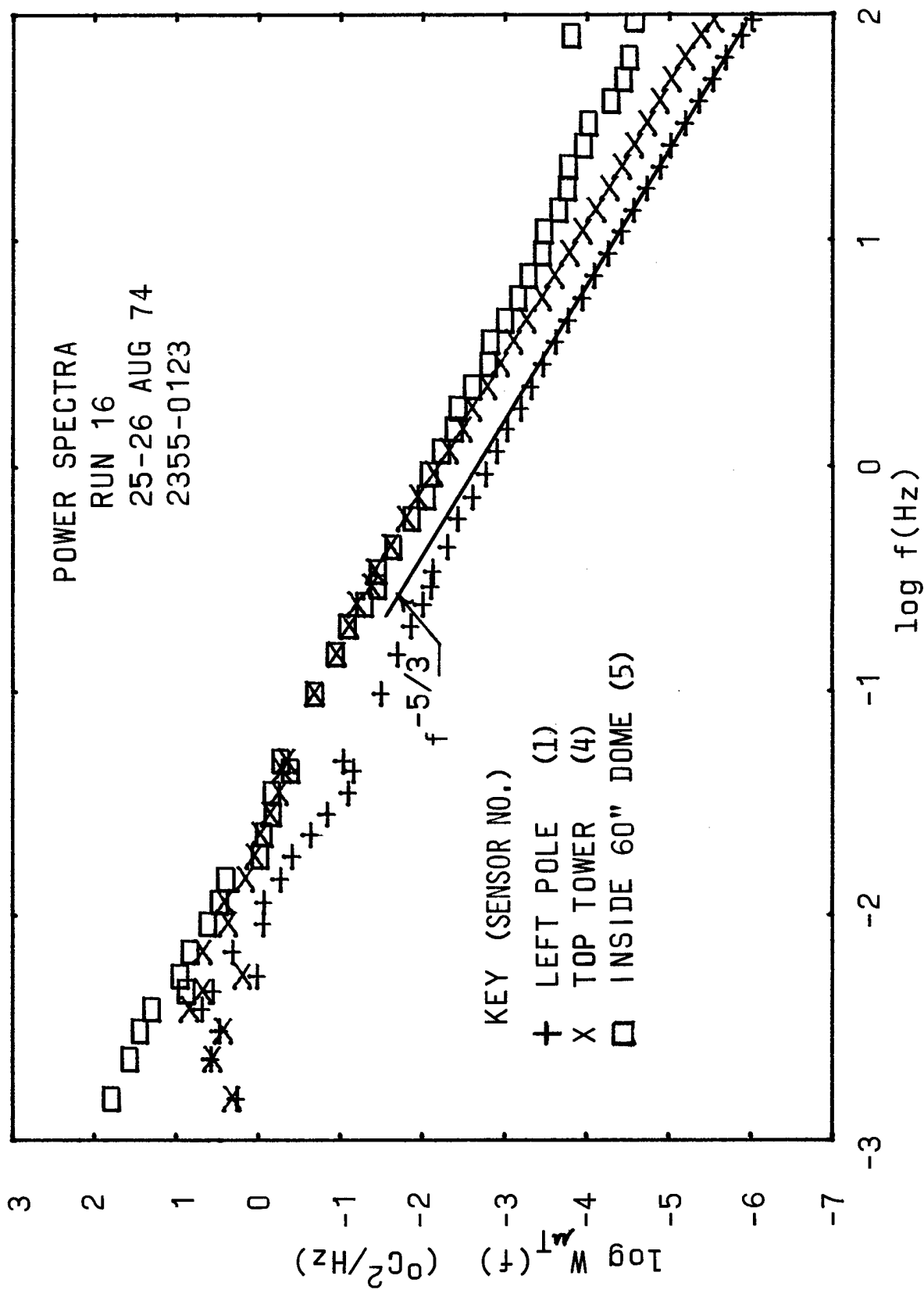


Figure 3. Power Spectra for Run 16 for microthermal sensors 1, 4 and 5.



To convert the standard deviation  $\sigma_T$  at an individual sensor to  $C_T^2$ , we use this equation:<sup>4</sup>

$$C_T^2 = 1.91 \sigma_T^2 L_0^{-2/3}. \quad (3)$$

The additional unknown here is the outer scale  $L_0$  and that is found from the probe pair mounted on the pole north of the dome (sensors 1 and 2). For that pair we know both  $\sigma_T^2$  (twice, since there are two sensors there) and  $C_T^2$ , and thus we know  $L_0$  via Eq. (3). In Fig. 4 we have plotted  $L_0$  for some selective runs over three days. We found that it changed little throughout a mission, as long as the sun neither rose nor set during that mission. For all the nighttime runs, the values of  $L_0$  ranged between 8 and 100 m.

We have encountered much discussion on this procedure of converting  $\sigma_T$  to  $C_T^2$ . The argument is basically that the value of  $L_0$  measured at the pole (sensors 1, 2) may not apply at the other sensor locations. First we must remind the reader that we *must* have values of  $C_T^2$  and not  $\sigma_T$  to do the optical propagation computations. Second, we checked very carefully the qualitative behavior of the  $\sigma_T$  plots (versus time) and the  $C_T^2$  plots so derived. We found that we could make exactly the same conclusions based on the  $C_T^2$  plots as we could with the  $\sigma_T$  plots. Third we found that the spectra, such as we show in Fig. 3, indicate large values of outer scale, although not necessarily so large near the dome surface as it is on the pole. Fourth, the values of outer scale as shown in Fig. 4 do not change so rapidly

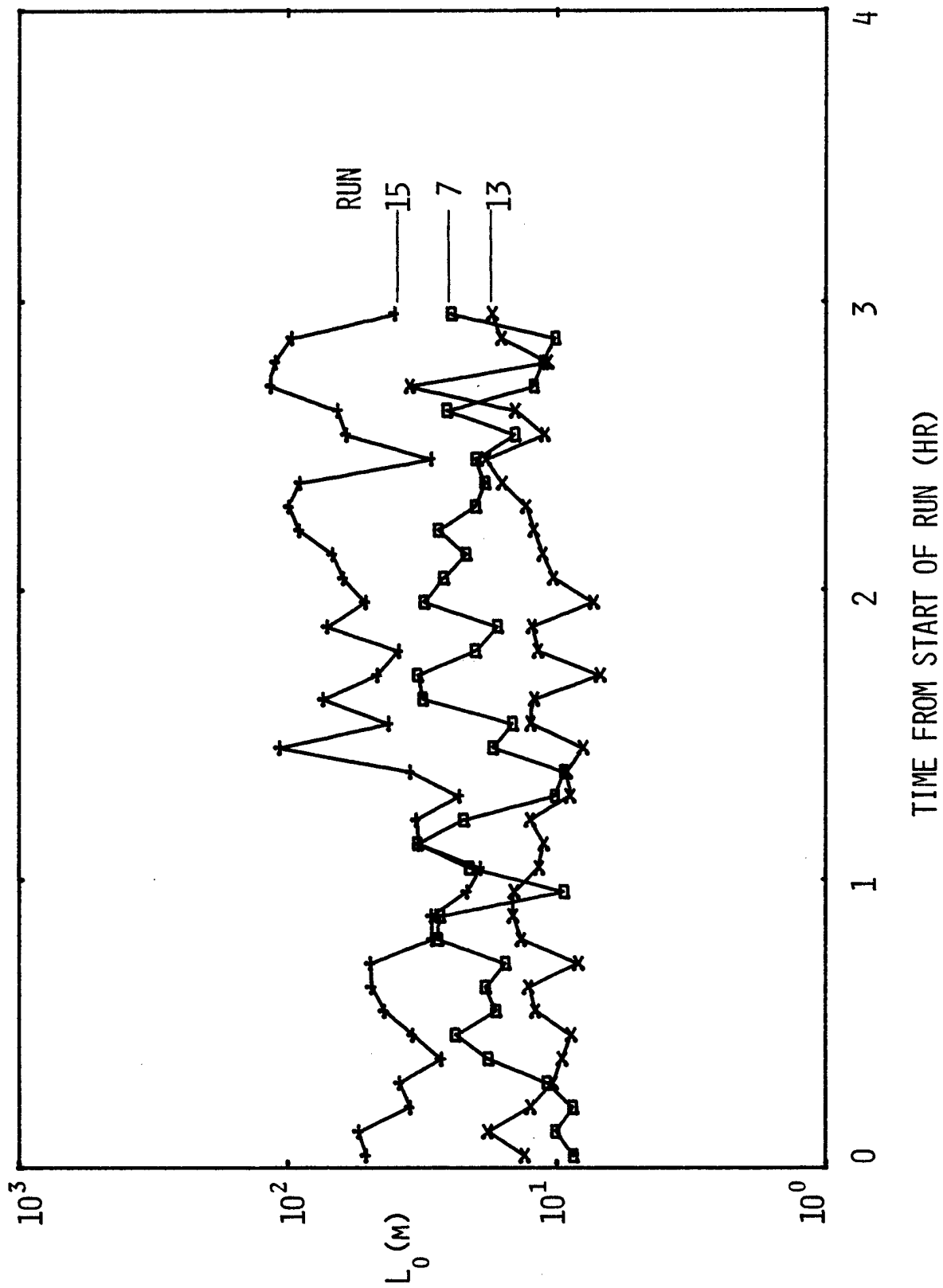


Figure 4. Outer Scale  $L_0$  versus time from start of mission for Runs 7, 13 and 15, on three different nights.

as to give an apparent change in  $C_T^2$  where a change had not occurred in  $\sigma_T$ . Finally, on limited runs we high-pass filtered the data so that all the sensor signals had the same cut-off frequency, and we recomputed  $C_T^2$ . This method gave values in good agreement with the method used here. We certainly accept the argument that the value of  $L_0$  as measured at the pole does not apply inside the telescope tube, but the signal levels there were so low as to almost be in the noise. We will show some tube data, but it is of very low strength.

#### D. Discussion of the Qualitative Nature of the Data.

We have plotted values of  $C_T^2$  versus time for those runs and sensors which we feel are significant. This includes Runs 3, 4, 7, 10, and 12-18. With the exception of Run 3, we have plotted  $C_T^2$  for sensors 1, 4, 5 and 6. In Runs 14-16 we have also provided  $C_T^2$  on sensors 6, 9 and 10, thus relating behavior at the 48" dome to the 60". In addition, for Runs 3, 4, 7, 16 and 17 we have reduced the facsimile plots from the sounder to a convenient format for comparison with microthermal data. All of this can be found in Figs. 5-18.

Let us direct our attention first to the facsimile records. The darkened areas on the records indicate regions from which back-scattered acoustic energy was received; i.e., regions within which fluctuating temperature gradients are sufficiently strong to produce detectable back-scatter. The distribution of these regions in space and time is extremely important

Figures 5-18. Plots of  $C_T^2$  and acoustic sounder returns versus time during the mission. (Remaining information on mission and a key are shown in each graph).

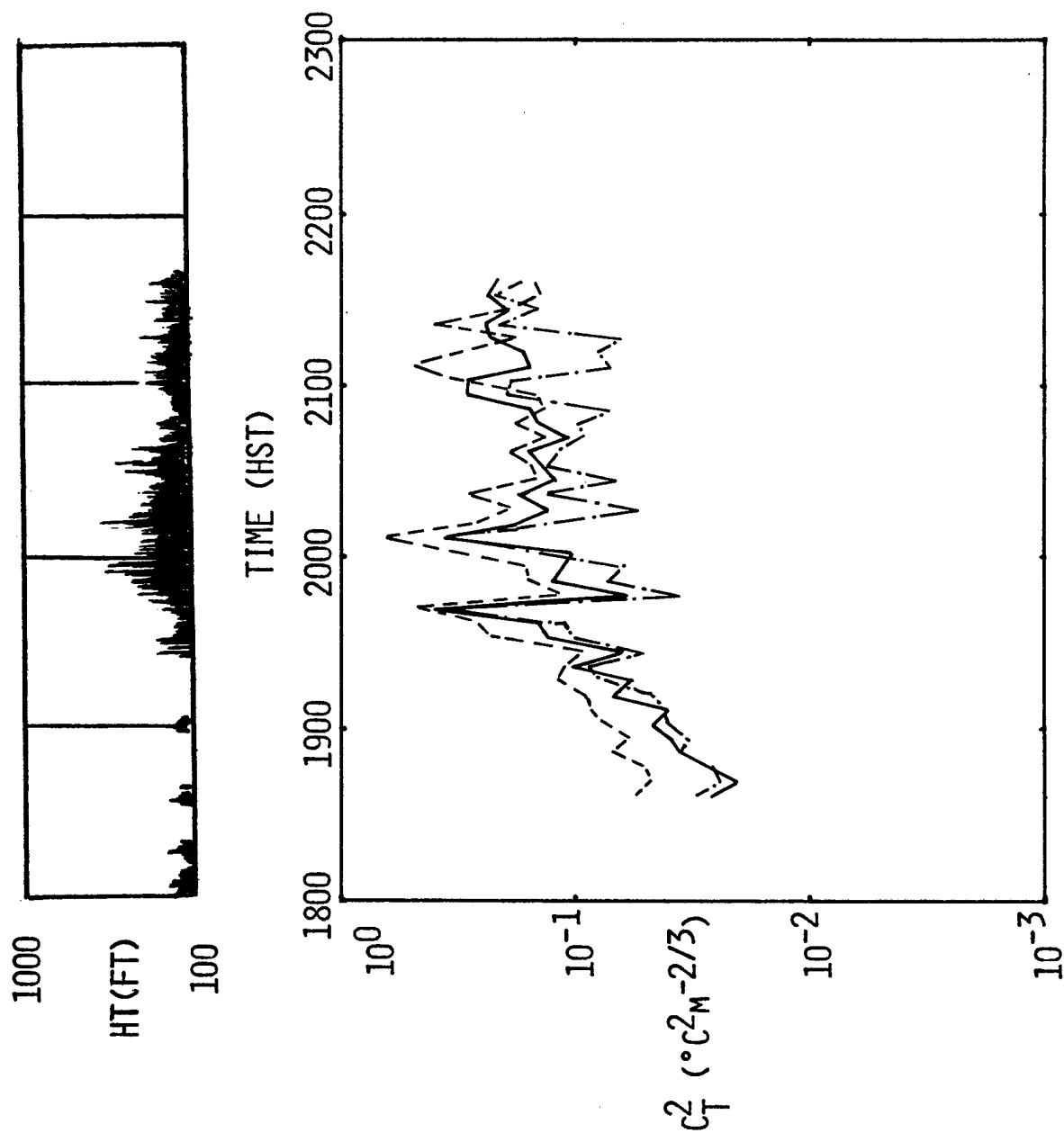
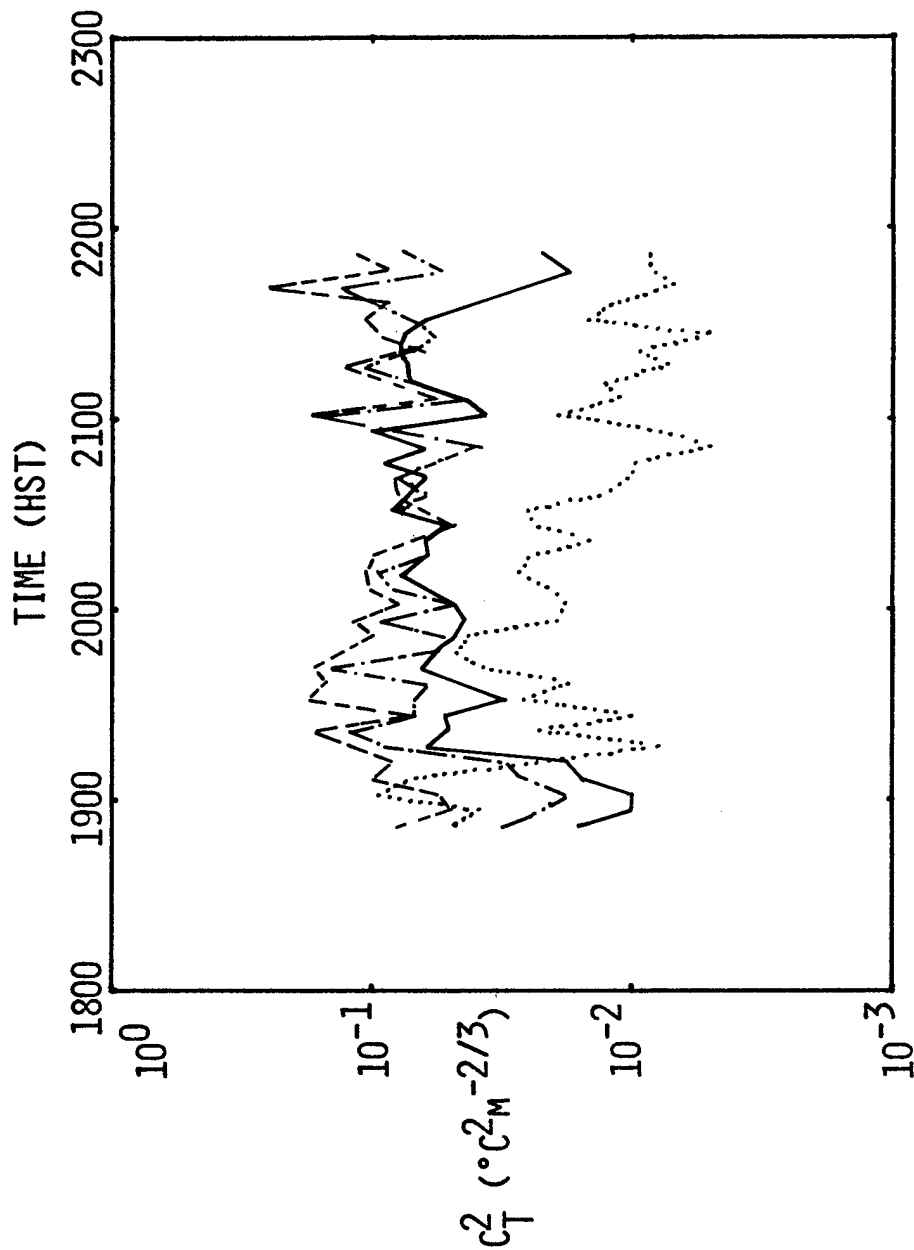
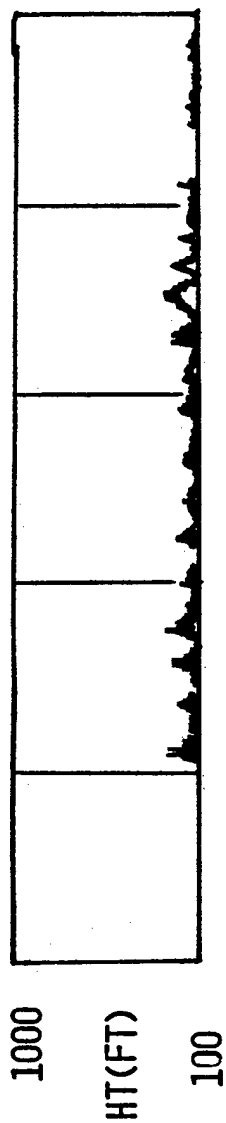


Figure 5



AMOS RUN 4  
21 AUG 74

ACTIVE SENSORS 1-8

WS 4M/SEC

WD SE

60" DOME NE

KEY (POSITION NO.)

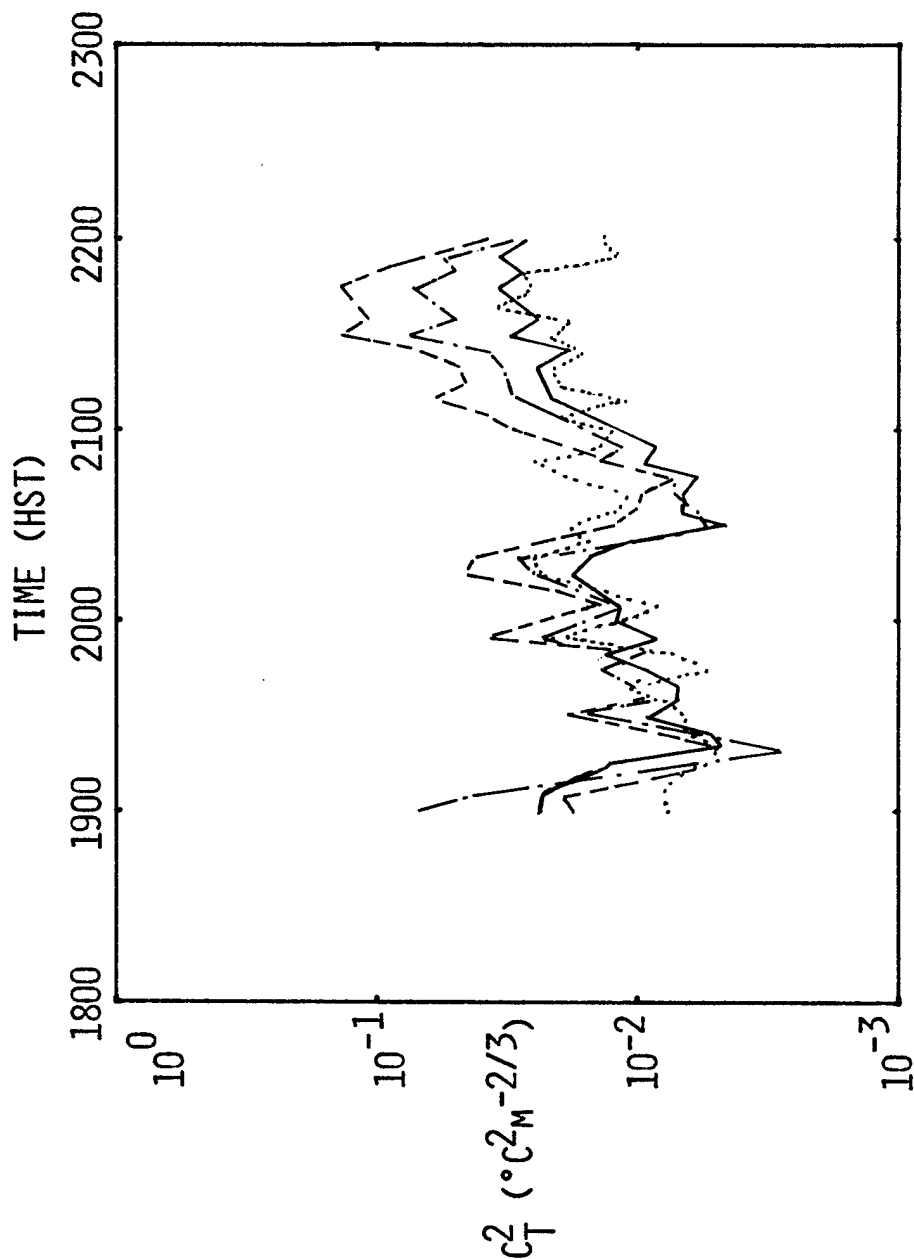
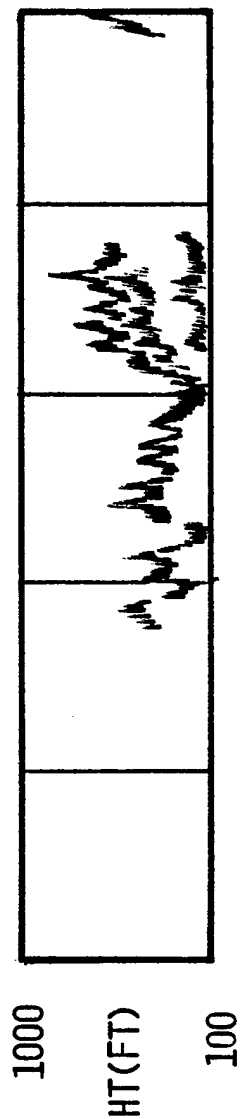
— POLE (1)

- - - TOP TOWER (4)

· · · · IN SLOT 60" (5)

- · - · OUT SLOT 60" (6)

Figure 6



AMOS RUN 7

22 AUG 74

ACTIVE SENSORS 1-8

WS 3M/SEC

WD S

60" DOME NE

KEY (POSITION NO.)

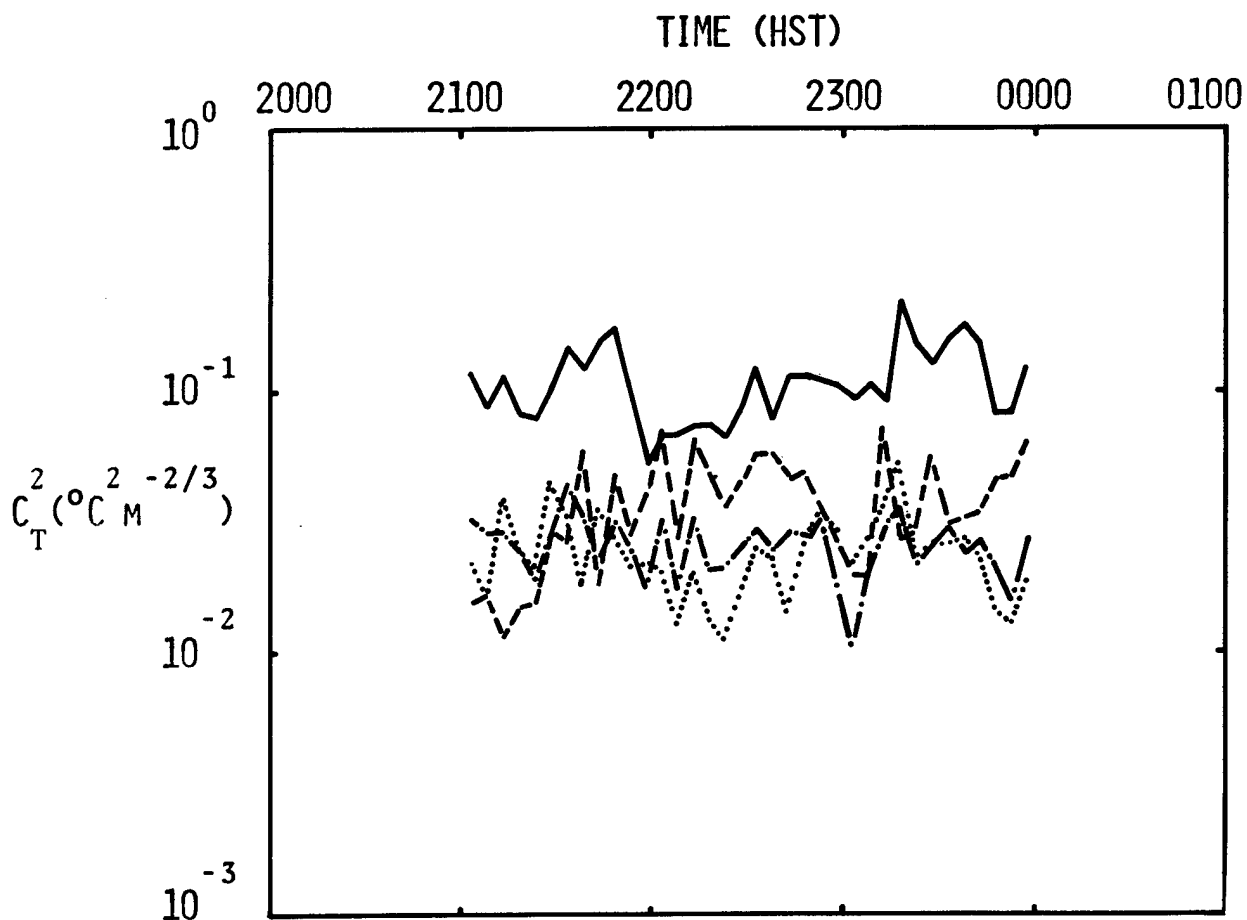
— POLE (1)

-- TOP TOWER (4)

..... IN SLOT 60" (5)

-.-.- OUT SLOT 60" (6)

Figure 7



AMOS RUN 10  
23-24 AUG 74

ACTIVE SENSORS 1-8

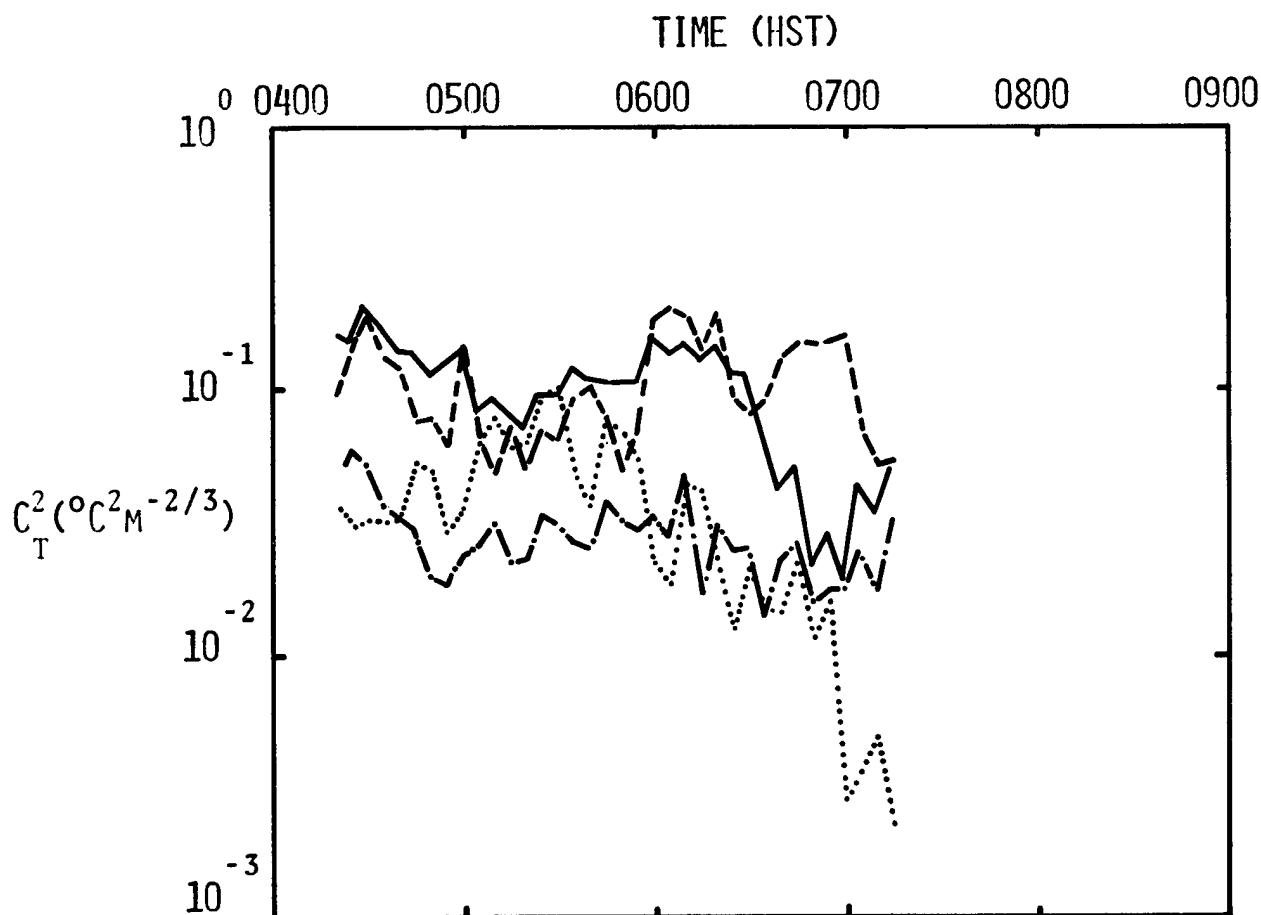
WS 2 M/SEC

WD NNW

KEY (POSITION NO.)  
 — POLE (1)  
 --- TOP TOWER (4)  
 ..... IN SLOT 60" (5)  
 —·— OUT SLOT 60" (6)

Figure 8





AMOS RUN 12

24 AUG 74

ACTIVE SENSORS 1-8

WS (NOT AVAIL)

WD NNW

60" DOME SSW

KEY (POSITION NO.)

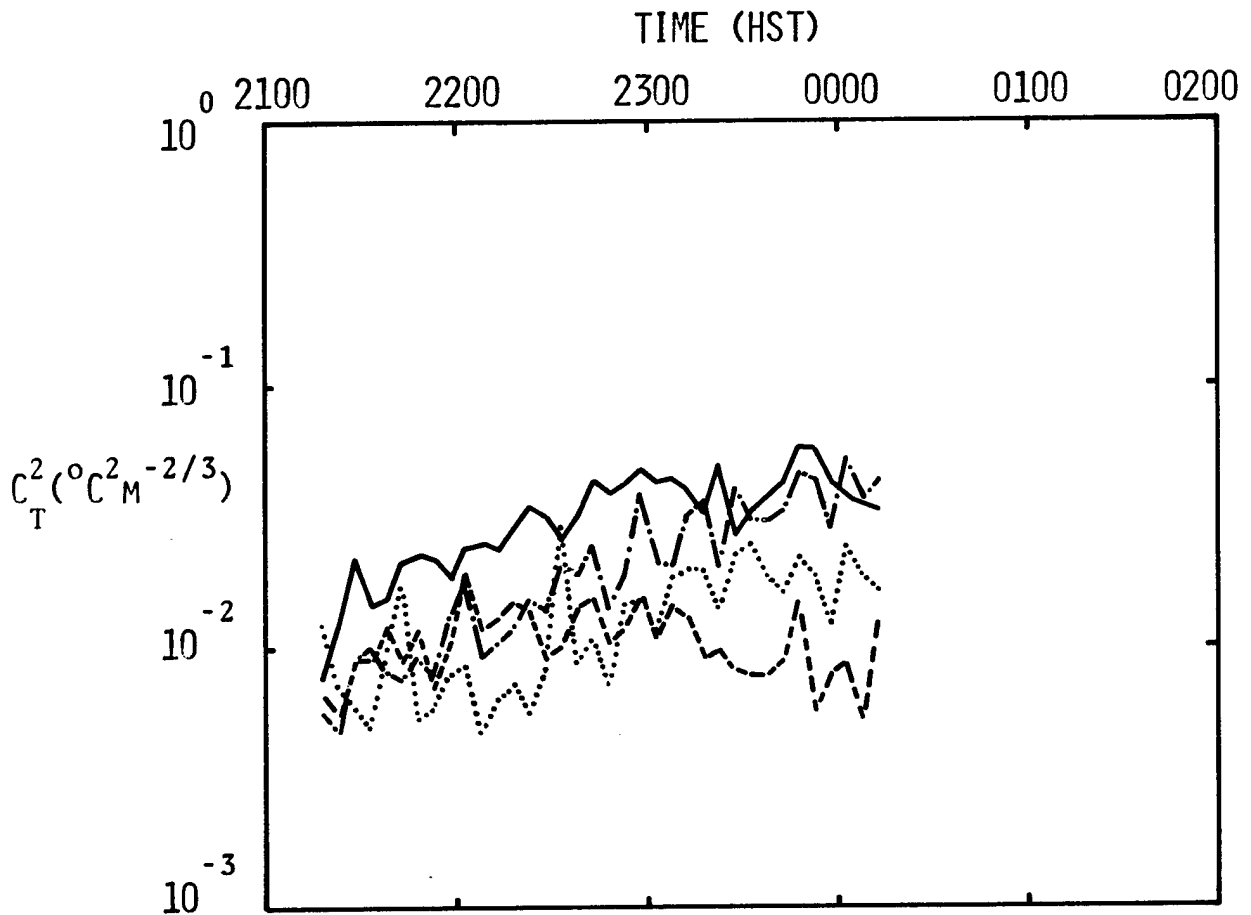
— POLE (1)

- - - TOP TOWER (4)

..... IN SLOT 60" (5)

- · - OUT SLOT 60" (6)

Figure 9

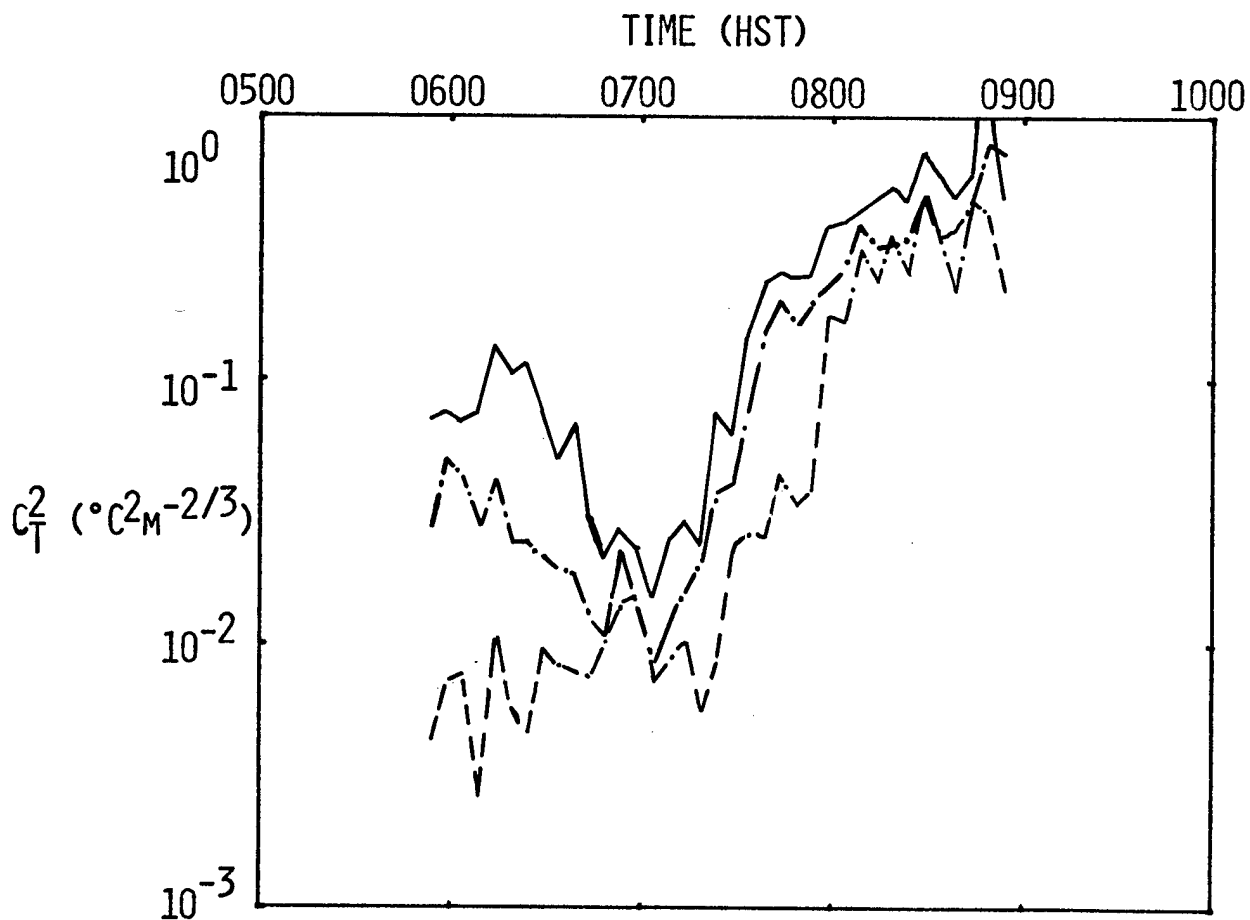


AMOS RUN 13  
24-25 AUG 74

ACTIVE SENSORS 1-10  
WS (NOT AVAIL)  
WD NNE  
60" DOME SSW  
48" DOME SSW

KEY (POSITION NO.)  
—— POLE (1)  
--- TOP TOWER (4)  
..... IN SLOT 60" (5)  
-.- OUT SLOT 60" (6)

Figure 10



AMOS RUN 14

25 AUG 74

ACTIVE SENSORS 1-10

WS 4M/SEC

WD NNE

60" DOME NE

48" DOME SSW

KEY (POSITION NO.)

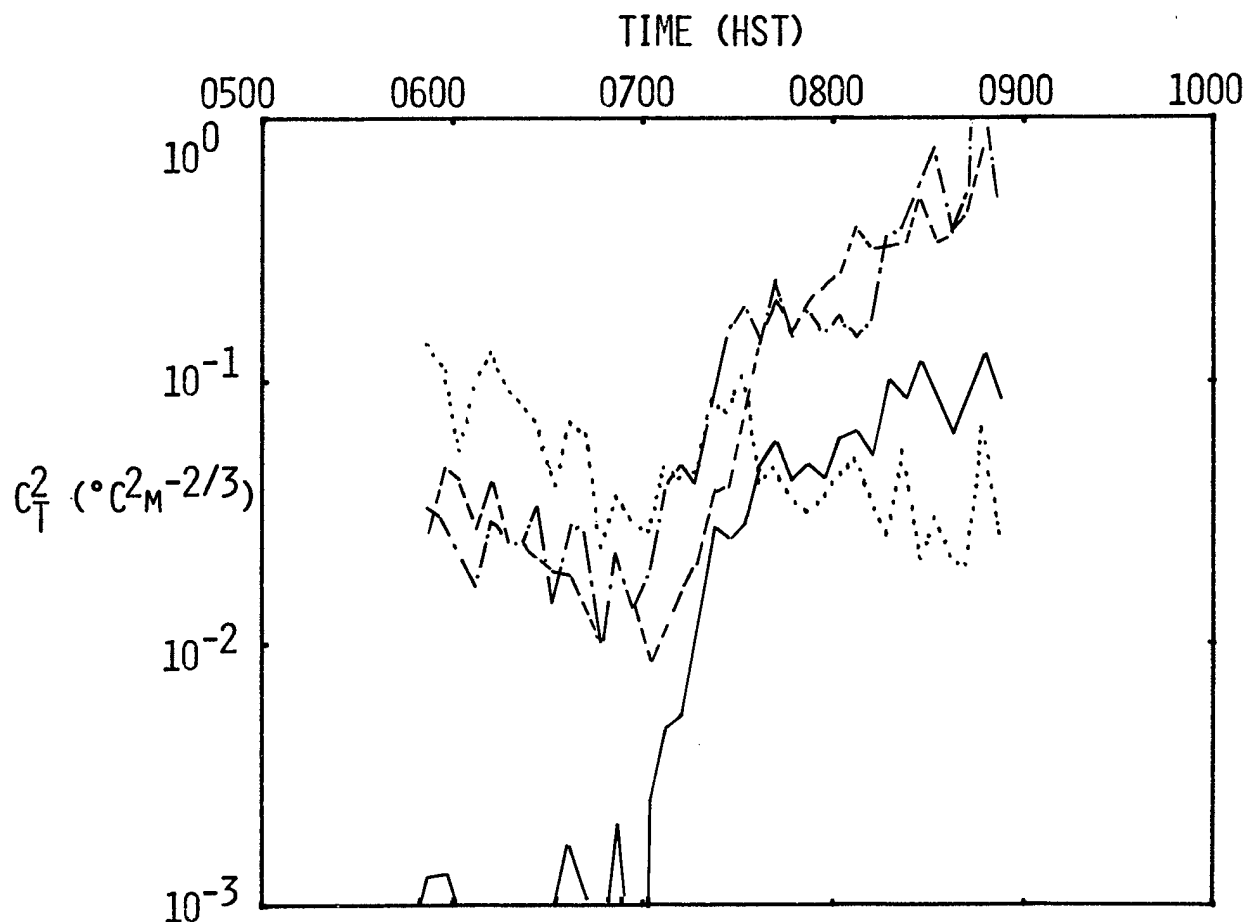
—— POLE (1)

--- TOP TOWER (4)

..... IN SLOT 60" (5)

— · — OUT SLOT 60" (6)

Figure 11



AMOS RUN 14

25 AUG 74

ACTIVE SENSORS 1-10

WS 4M/SEC

WD NNE

60" DOME NE

48" DOME SSW

KEY (POSITION NO.)

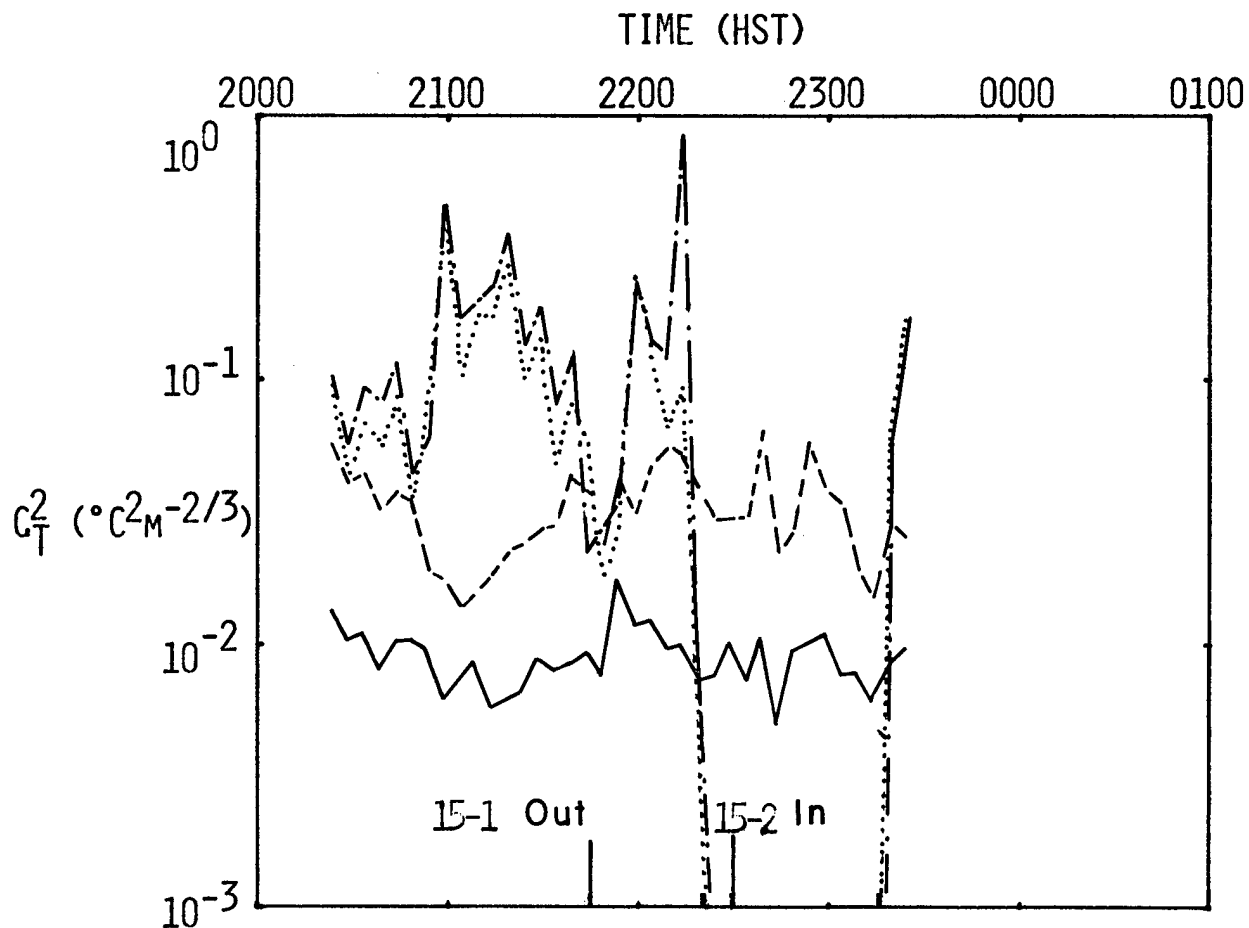
—— TOP 60" TUBE (8)

--- OUT SLOT 60" (6)

..... IN SLOT 48" (9)

- . - OUT SLOT 48" (10)

Figure 12



AMOS RUN 15  
25-26 AUG 74

ACTIVE SENSORS 1-10

WS 6M/SEC

WD S

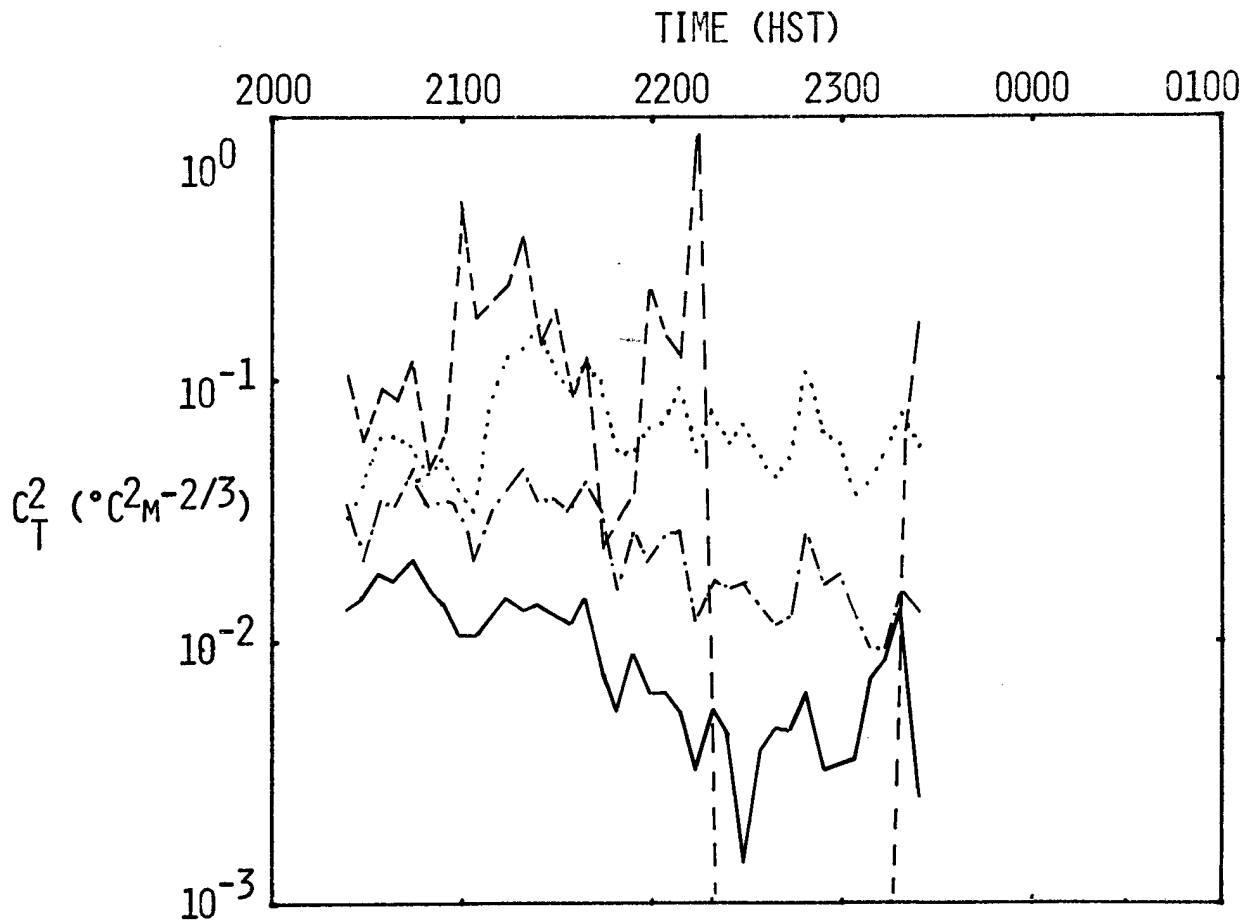
60" DOME NE

48" DOME SSW

KEY (POSITION NO.)

- POLE (1)
- - - TOP TOWER (4)
- ..... IN SLOT 60" (5)
- . - OUT SLOT 60" (6)

Figure 13



AMOS RUN 15

25-26 AUG 74

ACTIVE SENSORS 1-10

WS 6M/SEC

WD S

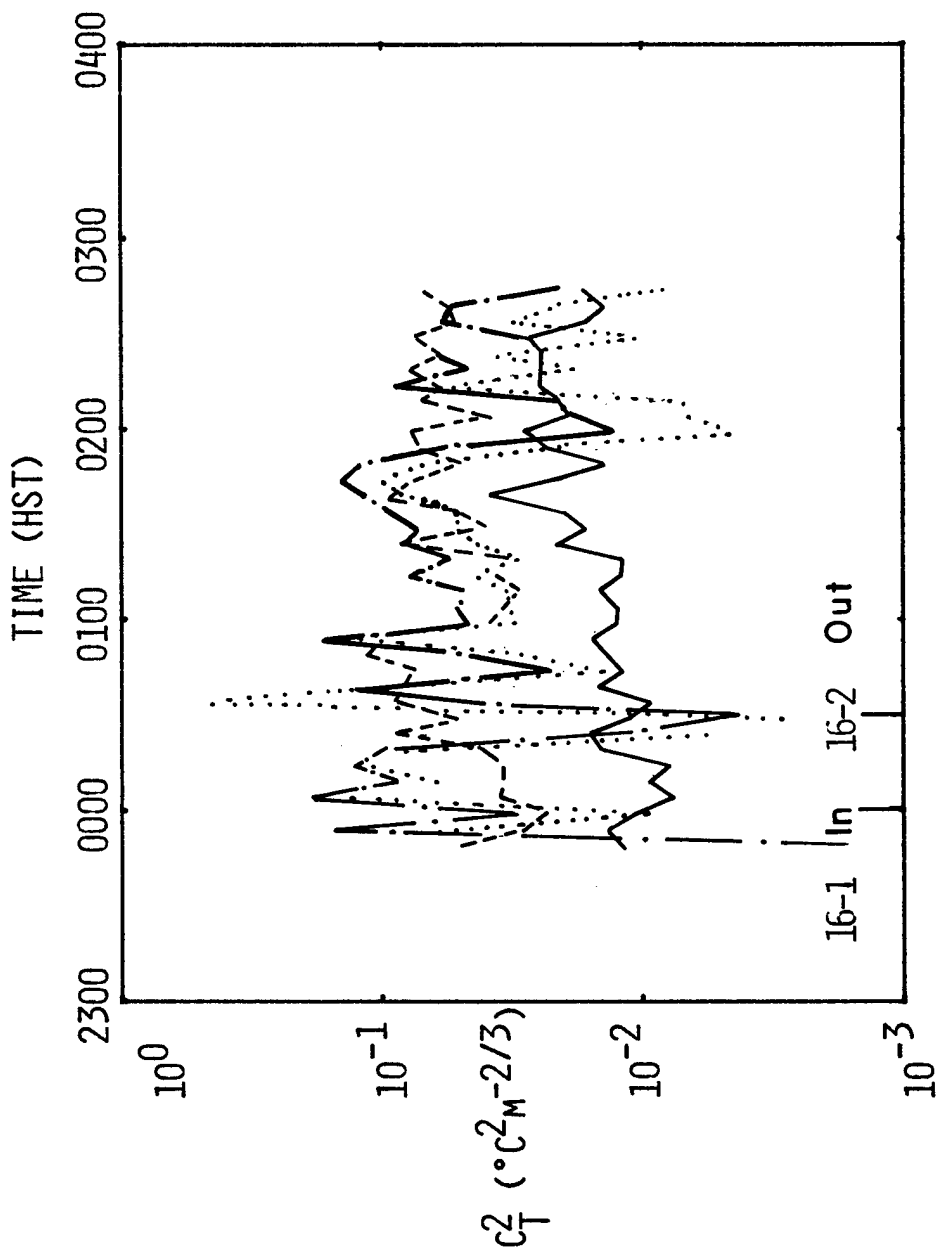
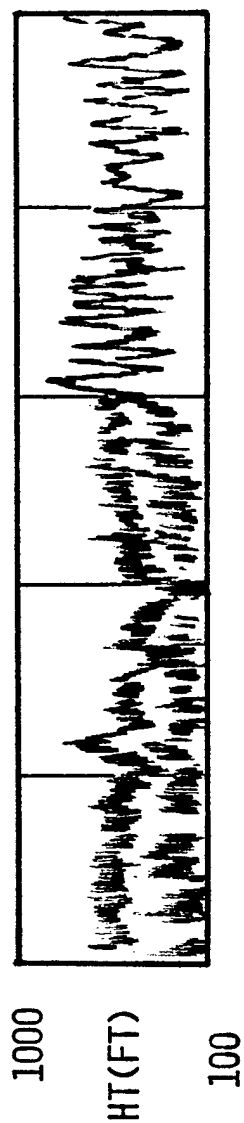
60" DOME NE

48" DOME SSW

KEY (POSITION NO.)

——	TOP 60" TUBE	(8)
---	OUT SLOT 60"	(6)
.....	IN SLOT 48"	(9)
- - -	OUT SLOT 48"	(10)

Figure 14



AMOS RUN 16

25-26 AUG 74

ACTIVE SENSORS 1-10

WS 6M/SEC

WD S

60" DOME NE

48" DOME SSW

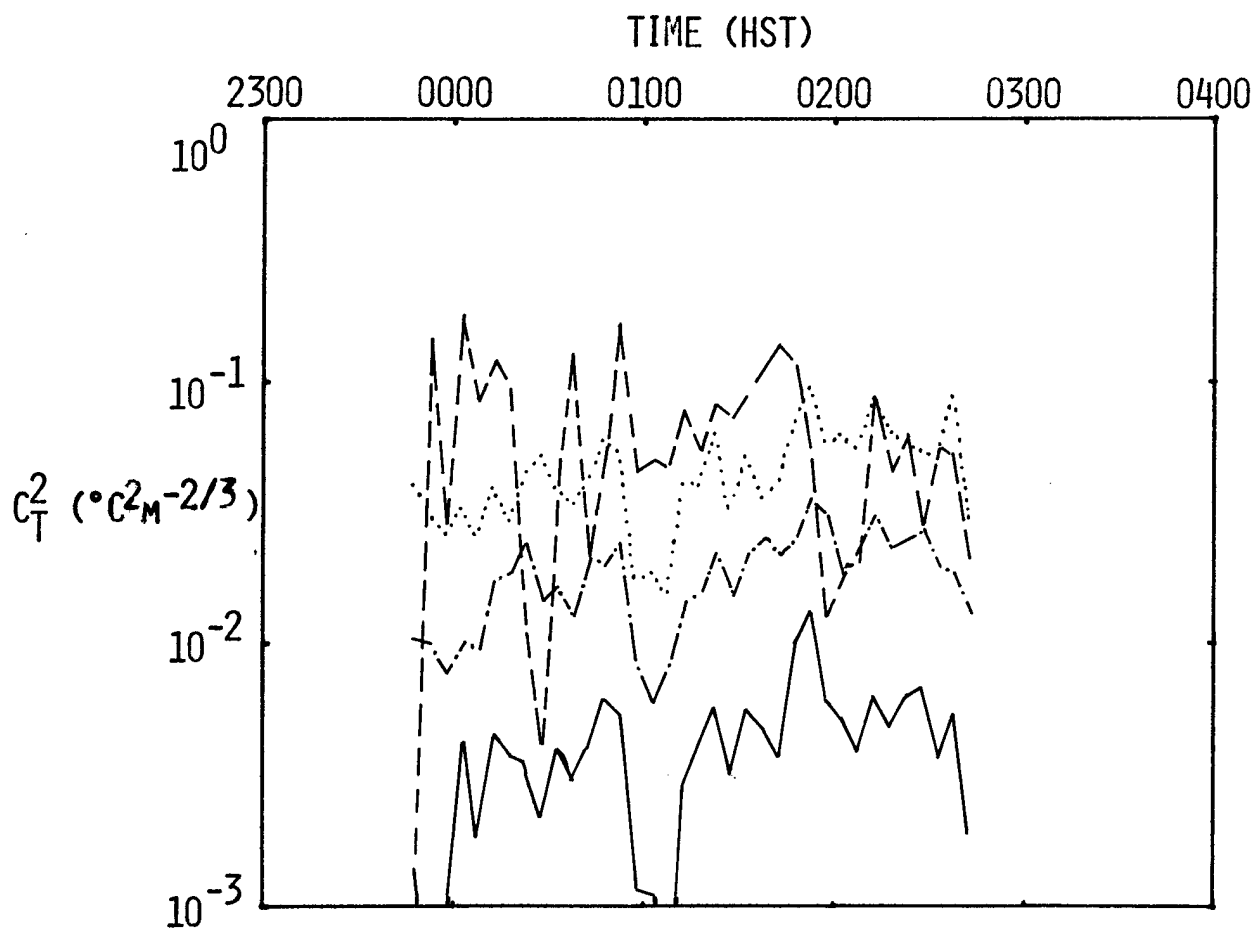
KEY (POSITION NO.)

— POLE (1)

-- TOP TOWER (4)

..... IN SLOT 60" (5)

--- OUT SLOT 60" (6)



AMOS RUN 16

25-26 AUG 74

ACTIVE SENSORS 1-10

WS 6M/SEC

WD S

60" DOME NE

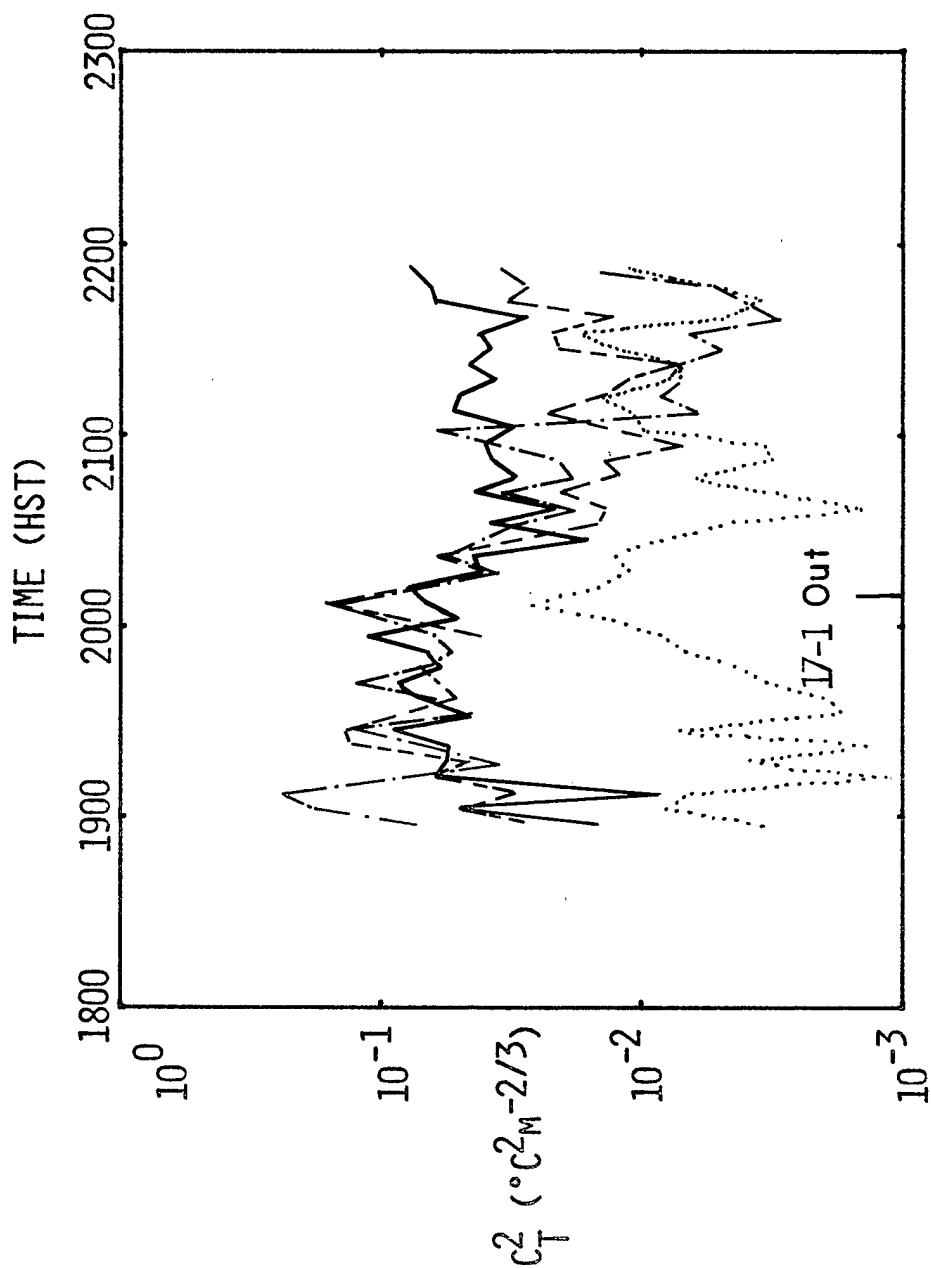
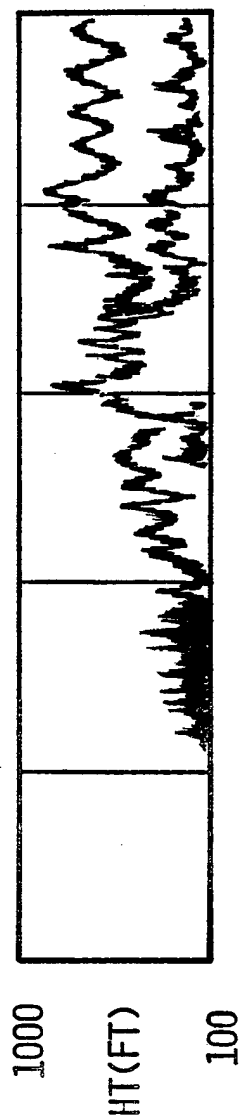
48" DOME SSW

KEY (POSITION NO.)

————	TOP 60" TUBE	(8)
-----	OUT SLOT 60"	(6)
.....	IN SLOT 48"	(9)
- . - .	OUT SLOT 48"	(10)

Figure 16





AMOS RUN 17  
26 AUG 74

ACTIVE SENSORS 1-8

WS 2M/SEC

WD S

60" DOME NE

KEY (POSITION NO.)

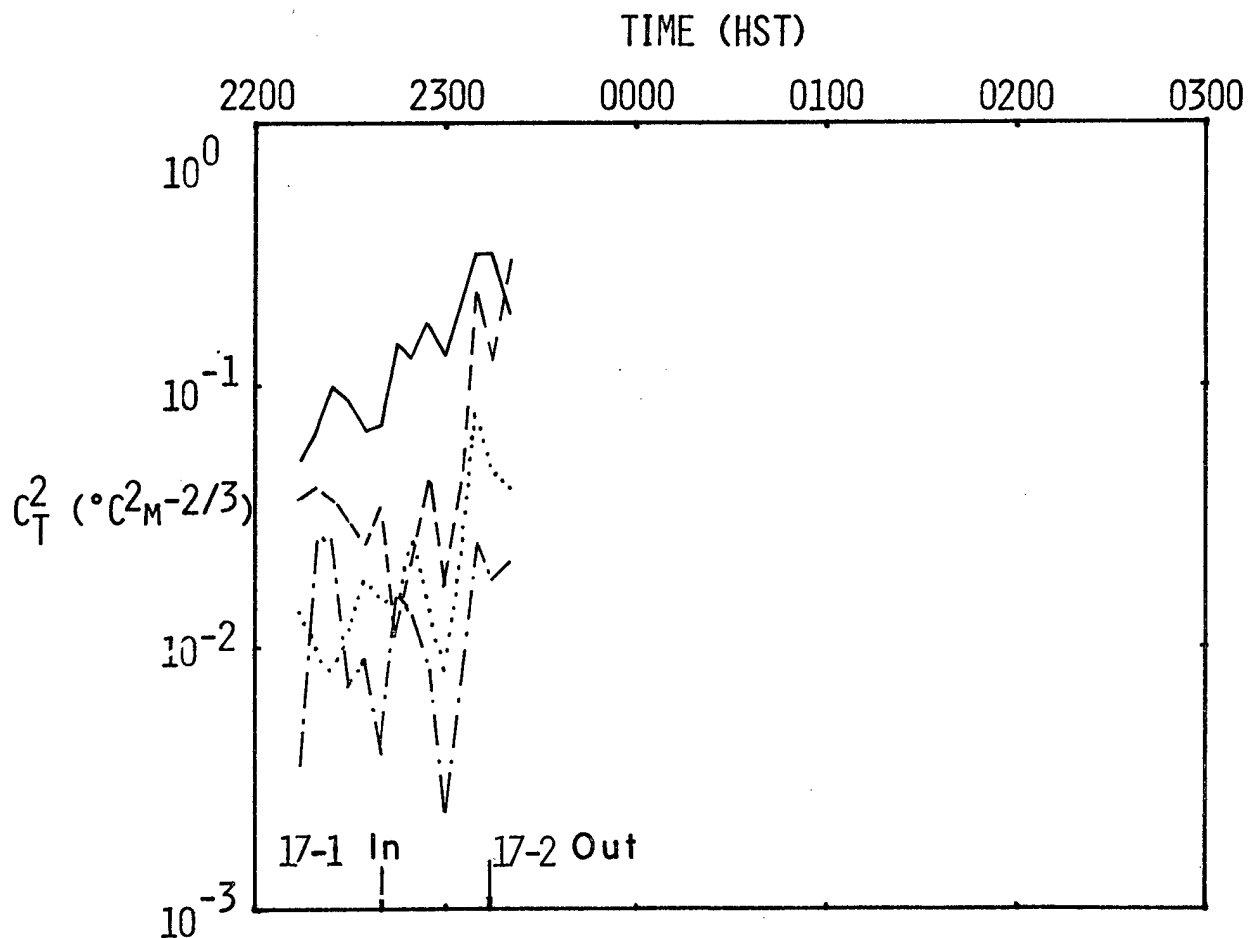
— POLE (1)

- - - TOP TOWER (4)

... IN SLOT 60" (5)

- · - OUT SLOT 60" (6)

Figure 17



AMOS RUN 18

26 AUG 74

ACTIVE SENSORS 1-8

WS 1M/SEC

WD S

60" DOME NE

KEY (POSITION NO.)

—— POLE (1)

--- TOP TOWER (4)

..... IN SLOT 60" (5)

-.-.- OUT SLOT 60" (6)

Figure 18

to characterizing the type of turbulent activity observed.

Shortly after sunset, a stable layer begins to develop over the mountain top. On windy nights, we observed strong sounder return over a substantial depth of the atmosphere above the surface. On calm nights, only a shallow inversion layer was observed. Regardless of surface wind conditions, gravity waves appeared and disappeared at levels throughout the sensing range of the sounder throughout much of each night. In general, all the features of the nighttime boundary layer observed over Mt. Haleakala are similar to those observed over any flat surface of the earth. The prime uncertainty we would express, based on the limited data presently available, is whether the depth of the boundary layer and the frequency of occurrence of windy and calm nights is also similar. Intuitively, one would expect a more shallow layer over the mountain peak on windy nights particularly, but more observations are required to permit analysis of this point.

Now, let us examine the plots of  $C_T^2$  with reference to the acoustic sounder records. It is clear that regions of intense activity above the observatory are frequently decoupled from regions of intense activity in the immediate vicinity of the dome, particularly under light wind conditions. For example, the  $C_T^2$  measurements near the dome showed large values only when the acoustic sounder also showed intense activity near the ground, not when the echoes were obtained from stratified layers

above the ground. Because of the strong decoupling that exists between these various layers at night, it is essential to determine seeing quality in some objective, quantitative manner at the same time the environmental observations are made.

#### E. Quantization in Terms of Seeing Degradation.

In the end, we will be comparing values of seeing degradation for all three sensors. The common parameter which we wish to use is Fried's coherence length  $r_0$ , defined for plane waves as

$$r_0 = \left\{ 0.423 k^2 \int_0^L C_n^2(z) dz \right\}^{-3/5}, \quad (4)$$

where  $k$  = wavenumber ( $2\pi/\lambda$ )

$L$  = pathlength

and  $C_n^2$  = refractive-index structure parameter.

If we can assume  $C_n^2$  is constant over the region  $0 \leq z \leq L$ , then

$$r_0 = [0.423 k^2 L C_n^2]^{-3/5}. \quad (5)$$

Furthermore if we have a slab model for our propagation medium with  $C_n^2$  constant in each slab, and if we calculate  $r_{0i}$  for each slab labeled  $i=1, \dots, N$ , then we may sum the  $r_{0i}$  in this manner:

$$r_0 = \left\{ \sum_{i=1}^N r_{0i}^{5/3} \right\}^{-3/5}. \quad (6)$$

Values of  $C_n^2$  are related to  $C_T^2$  by

$$C_n^2 = (79.2 \times 10^{-6} p/T^2)^2 C_T^2 \quad (7)$$

where  $p$  = pressure (mbar)

and  $T$  = temperature ( $^{\circ}\text{K}$ ).

The constant  $79.2 \times 10^{-6}$ , in units of  $^{\circ}\text{K}/\text{mbar}$ , is exact only for  $\lambda = 0.5 \mu\text{m}$ , in the middle of the visible, but varies little through the visible to infrared. Since the dependence of  $C_n^2$  on  $p$  and  $T$  is so weak for the range of  $p$  and  $T$  to be encountered we typically took  $p = 621 \text{ mbar}$  and  $T = 286^{\circ}\text{K}$ , so that

$$C_n^2 = 3.6 \times 10^{-13} C_T^2, \quad (\text{AMOS}). \quad (8)$$

Next we use  $r_0$  in computing a value of the seeing angle  $\beta$  as  $\lambda/r_0$ . This corresponds to the Rayleigh resolution angle for diffraction-limited performance  $1.22 \lambda/D$ , which we mentioned earlier. If we take  $\beta = 1 \text{ arc sec}$  as being sufficient to degrade imagery, then for visible wavelengths,  $r_0 = 0.11 \text{ m}$ . In turn Eq. (4) says that  $\int_0^L C_n^2(z) dz = 7.2 \times 10^{-13} \text{ m}^{1/3}$ . The biggest difficulty in interpreting this value for the microthermal probe data is in deciding upon the extent of the turbulence,  $L$ . Suppose we use the size of the dome,  $L = 10 \text{ m}$ . Then  $C_n^2 = 7.2 \times 10^{-14} \text{ m}^{-2/3}$  and after using Eq. (8),  $C_T^2 = 0.20 \text{ }^{\circ}\text{C}^2 \text{ m}^{-2/3}$ . We may consider this to be a "critical" value of  $C_T^2$  such that even if our  $C_T^2$  data approaches 0.20 we say that dome turbulence is significantly affecting seeing. In fact, if we refer to Figs. 5-18, we see this occurs in Runs 3, 4 and 12, where the turbulence appears to be naturally generated by the atmosphere; in Run 14, after sun-up; and during Run 15 where the turbulence appears to be

generated by the dome shell. Since the values of  $C_T^2$  do not exceed 0.20 for long periods of time, we may conclude that at times the turbulence generated by the domes is a degrading influence but not the consistently limiting factor.

We have computed values of  $r_0$  for all runs and all fine-wire sensors and these are tabulated in Table 3. This is perhaps the best place to judge the relative strengths of turbulence. We had to assume a value for  $L$ , so once again 10 m was taken. (We feel it is neither 3 nor 30 m. The dependence on  $L$  is  $L^{-3/5}$ , so if in the worst case the value of  $L$  is a factor of 3 off, then the  $r_0$  would change by a factor of 1/2.) We have placed parentheses around values of  $r_0$  inside the telescope tube, as the value of  $L_0$  which we have used is not appropriate there. These values are indicative, however, of the low strength of turbulence we noted inside the tube.

We can see in Table 3 that  $r_0$  is in the neighborhood of 0.1 to 0.2 m for a number of sensors during Runs 3, 4, 5, 6, 8, 10, 12, 14, 15 and 18. This indicates that the strength of local turbulence is often significant, but from these data we cannot tell if the source of turbulence is the dome structures. Since turbulence inside the 60" dome (Sensor 5) is consistently less than turbulence outside (Sensors 4 and 6) we can say that the turbulence is not coming from inside that dome. (Recall that a smaller  $r_0$  indicates more turbulence and a greater degradation.) The opposite is true of the 48" dome, in that consistently there

TABLE 3

Values of  $r_0$  (m) for microthermal probes assuming the extent of the turbulence  $L$  is 10 m. (If other values of  $L$  are of interest scale  $r_0$  according to  $L^{-3/5}$ .)

Sensor	Run 3	Run 4	Run 5	Run 6
1,2	0.13	0.25	0.34	0.29
3	0.16	0.24	0.23	0.19
4	0.11	0.17	0.17	0.11
5	-	0.41	0.39	0.52
6	-	0.21	0.21	0.16
7	-	(0.37)	(0.56)	(0.60)
8	-	(0.58)	(0.81)	(0.84)
9	-	-	-	-
10	-	-	-	-
Sensor	Run 7	Run 8	Run 9	Run 10
1,2	0.51	0.21	missing	0.16
3	0.44	0.20	-	0.27
4	0.30	0.27	-	0.30
5	0.52	0.16	-	0.39
6	0.38	0.14	-	0.38
7	(0.70)	(0.47)	-	(0.80)
8	(1.05)	(0.38)	-	(0.82)
9	-	-	-	-
10	-	-	-	-

TABLE 3 (Continued)

Sensor	Run 11	Run 12	Run 13	Run 14
1,2	missing	0.16	0.33	0.10
3	-	0.21	0.45	0.13
4	-	0.16	0.64	0.16
5	-	0.30	0.56	missing
6	-	0.36	0.41	0.13
7	-	(1.17)	(1.02)	(0.80)
8	-	(0.93)	(1.68)	(0.32)
9	-	-	0.14	0.23
10	-	-	0.25	0.12
Sensor	Run 15	Run 16	Run 17	Run 18
1,2	0.70	0.49	0.25	0.13
3	0.51	0.35	0.26	0.34
4	0.32	0.23	0.27	0.20
5	0.11	0.24	0.79	0.40
6	0.08	0.21	0.24	0.56
7	(0.45)	(0.74)	(0.89)	(0.70)
8	(0.68)	(1.10)	(1.40)	(0.37)
9	0.21	0.26	-	-
10	0.39	0.46	-	-

Note: Values for sensors 7 and 8 are only indicative of low turbulence in that the assumption on the value of  $L_0$  is undoubtedly incorrect.



is more turbulence inside (Sensor 9) than outside (Sensor 10).  
The 48" dome, unlike the 60", was in somewhat of an operational  
state, even though some equipment was turned off.

### III. ACOUSTIC SOUNDER CALIBRATED DATA

#### A. Background.

At the time the experiments were run at AMOS, the acoustic sounder had not undergone its final calibration. There was an additional unknown scale factor, hopefully a constant in altitude, which could only be determined by comparing the sounder output with values of  $C_T^2$  measured by microthermal probes such as we described in the previous section. This calibration was effected by the AFCRL Boundary Layer Branch during a remote experiment at Jackass Flats Nevada during October 1974. The results of that experiment will be presented in a separate article to be published later by AFCRL, but we have the salient remarks here. In addition AFCRL is currently preparing a report covering the use of an acoustic sounder in relation to optical propagation through turbulence.<sup>7</sup>

#### B. Calibration Set-up.

Three pairs of fine wire platinum resistance thermometers, spaced one meter apart, were mounted at heights of 150, 290 and 440 ft on the BREN tower at the AEC Nevada Test Site at Jackass Flats. These sensors were sampled at a rate of 20 times a second and recorded on digital magnetic tape using AFCRL's computer-controlled data acquisition system.<sup>8</sup> Sounder signals were recorded on analog tape as they were for the AMOS experiments. The antenna was located far enough upwind to avoid

reflections from the tower. Since its beam width is roughly  $45^\circ$ , this meant a separation distance of 1500 ft from the tower. Sensors were not placed above 440 ft since the environment in Nevada is very dry and thus only noisy returns were sensed above about 500 ft.

#### C. Brief Remarks on Theory of Operation.

A recent report by Neff<sup>9</sup> contains a thorough treatment of the subject of acoustic sounders in measuring temperature fluctuations. The report has extensive references for those who are interested. The fundamental concepts are based on the fact that sharp discontinuities in the temperature or wind field will cause acoustic energy to be scattered or deflected from the propagation direction. In the backscatter direction (scattering angle of  $180^\circ$  from the propagation), the scattered energy is theoretically a function only of the temperature fluctuations. The theory also assumes that the scale size of the turbulent fluctuations causing the scatter is within the inertial subrange, thus providing a relationship between the backscatter cross-section and  $C_T^2$ , the temperature structure function.

#### D. Results of Calibration at Nevada.

To obtain statistically stable estimates of  $C_T^2$  from the acoustic sounder and microthermal probes, we chose periods with fully developed convection when the turbulence is reasonably stationary and the atmospheric boundary layer is well mixed.

One-hour averages of  $C_T^2$  were computed for each of the three heights.

Separate comparisons were made for each of the three heights to determine whether the derived calibration factors were invariant with height. Let us define a simple relation between the two values of  $C_T^2$  measured as

$$C_{T(\text{Tower})}^2 = \alpha C_{T(\text{Sounder})}^2 \quad (9)$$

The following values of  $\alpha$  were obtained for unstable conditions:

$\alpha = 1.83$ , for 150 ft altitude

$\alpha = 2.33$ , for 290 ft altitude

and  $\alpha = 2.89$ , for 440 ft altitude.

Calibration factors for slightly stable cases characterized by light to moderate winds and good mixing were

$\alpha = 0.86$ , for 150 ft altitude

$\alpha = 0.93$ , for 290 ft altitude

and  $\alpha = 1.03$ , for 440 ft altitude.

The strong height dependence of the calibration factor  $\alpha$  for unstable conditions, and the marked difference in  $\alpha$  between convective (unstable) and stable conditions were unexpected and puzzling. The results suggest an unaccounted loss of acoustic energy that is apparently considerably more severe during unstable than stable conditions as well as the possibility of a

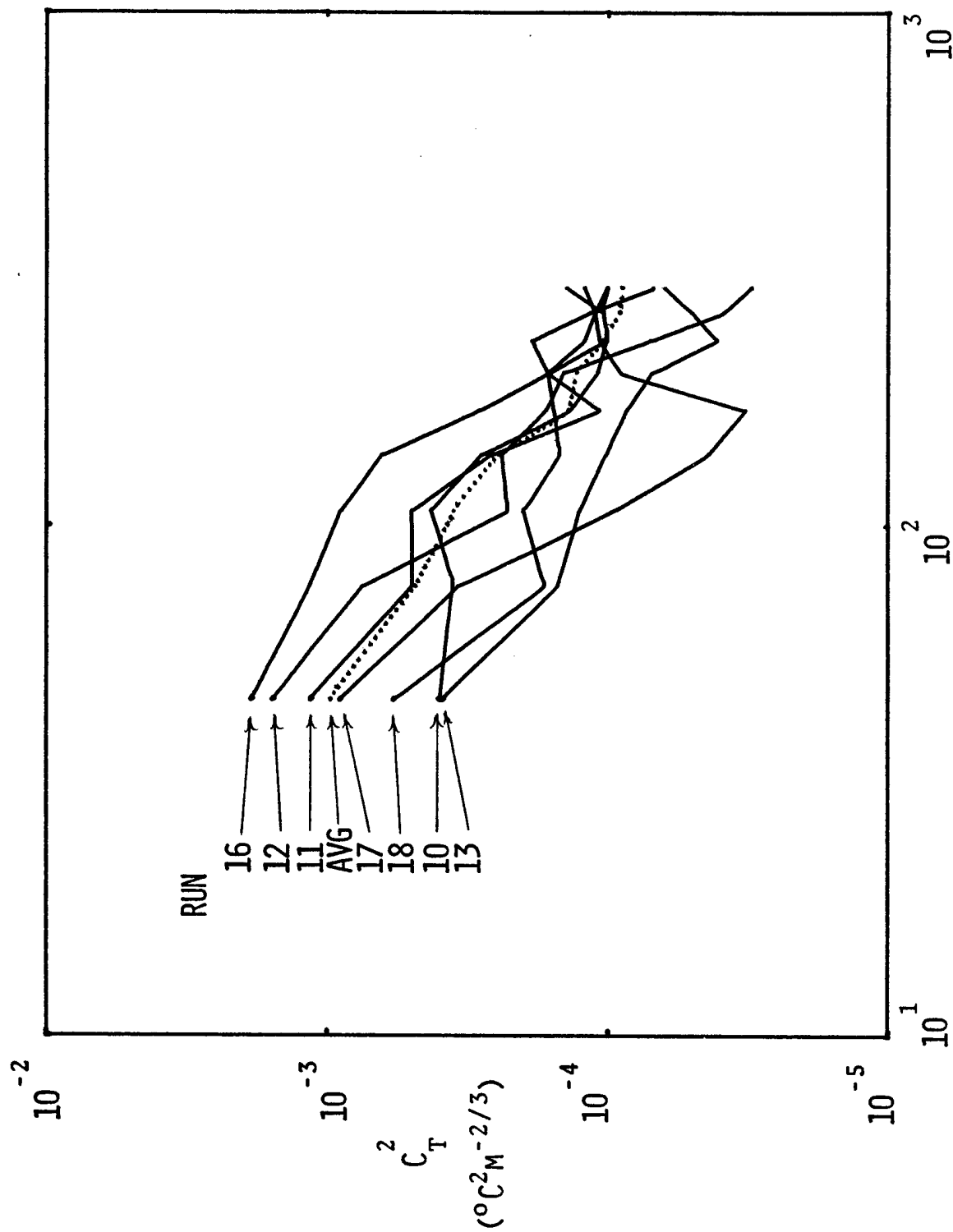
different scattering mechanism under stable conditions. Speculation as to why the calibration factor varies is given in AFCRL's report,<sup>7</sup> but there is not yet a conclusive explanation.

It should, of course, be noted that the immediate application of the echo sounder at AMOS is for optical tracking problems under stable conditions for which results show only a weak height dependence. This is, indeed, a fortuitous result for it permits a quantitative analysis of the AMOS data on a rational basis even though a full explanation of the scattering phenomena is yet to be presented. For our purposes, we will use a value of 1.00 for  $\alpha$ .

#### E. Description of AMOS Data.

As already mentioned, all the AMOS experiments were conducted under thermally stable conditions. The sounder was operated at a frequency of 2000 Hz; the pulse length selected was 50 msec; the delay time was set at 150 msec; and the pulse repetition rate was roughly 30 per minute. This gave a height range of roughly 305 m (1000 feet). Surface measurements of pressure, humidity, and temperature were obtained with a barograph and a hygro-thermograph. Relative humidities were generally 40% or higher at all times, thus the increased effective range with respect to Nevada. Lower relative humidities (10 - 20%) were observed only in the daytime during the course of these experiments.

Values of  $C_T^2$  were computed at 100 ft intervals from 150 to 950 ft for successive one-minute averaging periods. Rather than averaging over a 100 ft region (e.g. 100 to 200 ft), we have averaged only over an altitude band of approximately 50 ft. centered at the indicated levels. These values are tabulated for Runs 10-14 and 16-18 in the AFCRL report.<sup>7</sup> (Other runs were found to be too noisy.) Here we present averages for the entire run in Fig. 19 and in Table 4. Averaging times for these runs are the same as given in Table 2. Rather than to view plots of Fig. 19 as averages profiles, we prefer to think of them as the probability of locating a layer at a certain altitude, but in the units of  $C_T^2$ . Note there is an increasing probability of having a layer occur at altitudes near the top of the mountain rather than higher up. Indeed the rate of decay with altitude for the average overall runs (excluding Run 14 which extended through sun-up) is quite steep, in that it goes as  $0.19z^{-1.37}$ , with  $z$  in meters. This behavior was found by performing a least squares fit to the average profile and had a correlation coefficient "r" of 0.9929. In the boundary layer at night, under stable conditions, the dependence is  $z^{-2/3}$ ; whereas during the day, in convective unstable conditions, the dependence is  $z^{-4/3}$ . This suggests that the presence of the mountain has an influence on the stratification of the turbulence. We further suppose that the region of 100 to 1000 ft above the mountaintop is not necessarily indicative of what occurs above 1000 ft. That is, one should not take the  $z^{-1.37}$  profile too seriously outside the measurement range.



ALTITUDE ABOVE SITE  $z(m)$

Figure 19. Profiles of Turbulence for Runs 10-13 and 15-18 as sensed by the acoustic sounder. Also shown is the average of these profiles.

TABLE 4

Values of integrated  $C_n^2$  and coherence length  $r_0$  for the acoustic sounder profiles.

Run	$\int C_n^2 dz \text{ (m}^{-1/3}\text{)}$	$r_0 \text{ (m)}$
10	$2.20 \times 10^{-14}$	0.89
11	$3.34 \times 10^{-14}$	0.69
12	$3.53 \times 10^{-14}$	0.67
13	$1.18 \times 10^{-14}$	1.29
14	$2.87 \times 10^{-14}$	0.76
16	$5.83 \times 10^{-14}$	0.50
17	$2.02 \times 10^{-14}$	0.94
18	$1.91 \times 10^{-14}$	0.97
Avg	$2.86 \times 10^{-14}$	0.76



#### IV. OPTICAL MEASUREMENTS

##### A. Experimental Technique.

It was essential for the experiment to include one instrument which provided an integrated measure of turbulence for the entire atmosphere. The instrument should measure optical phase, or phase-related quantity such as arrival angle. Amplitude scintillation is not sufficient because that is affected more by high altitude turbulence and hardly affected by low altitude turbulence at all. The most reliable measurement is of arrival angle difference, which is not affected by telescope tracking errors. An analysis of this measurement is provided by Fried.<sup>10</sup>

The instrument itself must be portable and be capable of providing short exposure, quantitative results. Portability is required so that seeing conditions as viewed from inside and outside the dome can be investigated. The data must be of short exposure (less than roughly the 25 msec time constant of the atmosphere) so that the fluctuations in arrival angle do not cause a blur in the recorded data. Obviously quantitative data are required so that comparisons with other instruments can be made. Hence we have avoided subjective measures such as were done in the original site survey.

The measurements were made on a small telescope which had fitted over the aperture a Hartmann mask consisting of two holes.

To measure arrival angle at the individual subapertures, the telescope was pointed at a bright star, and the images of the star for the two subapertures were recorded on film. To achieve sufficient separation of the images on the film, the telescope was slightly defocused. We describe the procedure analytically in Appendix A.

#### B. Instrument.

The instrument chosen for use in this experiment was a Questar Seven. This telescope is a Maksutov Cassegrain Catadioptric system with a clear aperture of 7 inches, obscuration ratio of 0.34 and a prime focal length of approximately 112 inches. In order to increase the image motion a minus 66.06 mm FL Barlow Lens was used to provide a 2X magnification. An assortment of Questar accessories was also used in order to obtain a fully portable instrument capable of sidereal tracking. A schematic diagram of the device is in Fig. 20.

Data recording was accomplished by use of a Questar-modified Nikon F 35mm camera body. This camera was equipped with a 250 exposure motorized film drive. However, film advancement and shutter release were performed manually in order to avoid excessive vibration. Kodak RAR 2484 film was used to record the images. Processing was carried out for two minutes at 94°F in D-19 developer.

Two Hartmann plates were constructed from extra lens

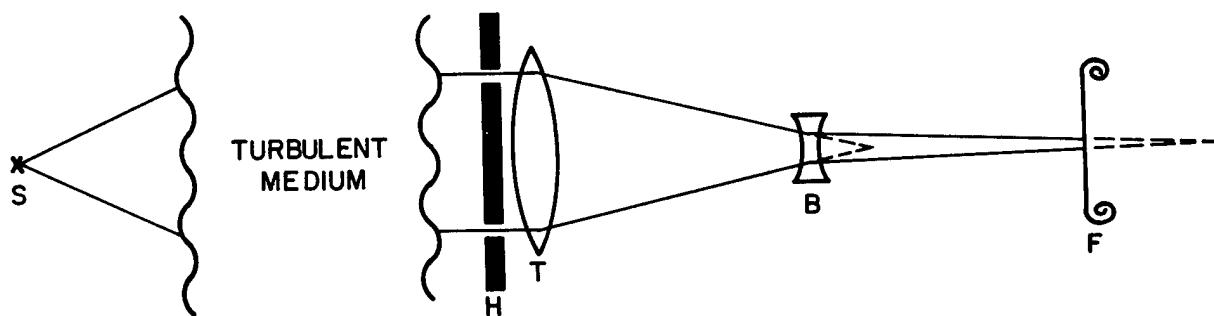


Figure 20. Schematic Diagram of Optical System Showing Source S, Telescope T, Hartmann Plate H, Barlow Lens B, and Film F.

caps. One contained three 2.25 inch diameter holes at two different spacings. At times this mask had one of the three holes covered. The second contained six 1.0 inch holes at five different spacings.

### C. Measurements.

Data were collected at AMOS during the period 19 August to 31 August 1974. A summary of all data runs attempted is given in Table 5. In all, data were taken at three different locations: inside the east dome of the observatory, in the aircraft spotters enclosure approximately fifty feet north of the observatory and on top of Red Hill (highest point on the mountain). These locations are indicated in Figs. 1 and 2. Of the twenty-eight data runs attempted, two were exposure sequences, two were taken with the 1.0 inch aperture plate and twenty-four were taken with the 2.25 inch aperture plate. Of these last twenty-four, five produced no data due to camera malfunction or excessive vibration. Thus there is potentially good data from nineteen runs with this plate.

These data can potentially result in information relative to the following:

1. Comparative seeing inside and outside of the dome.
2. Comparative seeing inside the dome and at Red Hill.
3. Correlation with the acoustic and microthermal data.
4. Comparative seeing inside the dome with different angles between the dome slot and the wind direction.

TABLE 5. OPTICAL DATA SUMMARY

Date Time	Data ID	Location <sup>(1)</sup>	Hartmann <sup>(2)</sup> Plate	Object; θ EL	Comments
8/22 0030	ESNB	Outside	2	Vega	Exposure sequence
8/23 0030	8-1	Outside	1,3	Vega	Exposure sequence and 25 frames of Hartmann data
8/23 2200	-	Outside	1	Vega	No data: vibration in motor drive
8/23 2300	-	Outside	1	Vega	No data: vibration in motor drive
8/24 0100	-	Outside	1	Altair	No data: camera malfunction
8/24 2200	13-1	Outside	1	Vega, 67°	Acoustic and microthermal data
8/24 2300	13-2	Outside	1	Altair, 75°	Acoustic and microthermal data
8/24 2330	13-3	Outside	1	Altair, 68°	Acoustic and microthermal data
8/25 0015	13-4	Outside	1	Altair, 58°	Acoustic and microthermal data
8/25 2145	15-1	Outside	1	Vega, 65°	Acoustic and microthermal data partial data loss due to power failure during development
8/25 2230	15-2	Inside	1	Vega, 58°	Acoustic and microthermal data
8/26 0000	16-1	Inside	1	Altair, 55°	Acoustic and microthermal data only 70 frames due to wrong focus
8/26 0030	16-2	Outside	1	Altair, 48°	Acoustic and microthermal data
8/26 2010	16-3	Outside	3	Vega, 72°	Acoustic and microthermal data
8/26 2045	-	Outside	1	Vega, 72°	No data: camera malfunction
8/26 2130	-	Inside	1	Vega, 70°	No data: camera malfunction
8/26 2240	17-1	Inside	1	Vega, 60°	Acoustic and microthermal data only ≈ 90 frames
8/26 2315	17-2	Outside	1	Vega, 54°	Acoustic and microthermal data

TABLE 5. (cont'd)

Date Time	Data ID	Location (1)	Hartmann (2) Plate	Object; θ EL	Comments
8/27 2100	19-1	Outside	2	Vega, 72°	One Hartmann aperture blocked
8/27 2130	19-2	Inside	2	Vega, 69°	Further activity suspended due to power failure
8/29 2030	20-1	Inside	2	Vega, 72°	Wind ≈ 45° off slot
8/29 2130	20-2	Inside	2	Vega, 68°	Wind ≈ 135° off slot
8/29 2200	20-3	Inside	2	Altair, 78°	Slot down wind
8/29 2215	20-4	Inside	2	Altair, 75°	Slot up wind
8/30 2045	21-1	Red Hill	2	Vega, 72°	Outside visitors center, not in wind shadow
8/30 2130	21-2	Red Hill	2	Vega, 68°	Same location as case 21-1
8/30 2245	21-3	Inside	2	Altair, 78°	
8/30 2300	21-4	Inside	3	Altair, 75°	

Notes: (1) Outside: Aircraft spotters enclosure except for case ESNB.  
 Inside: East dome (60" dome).  
 Red Hill: Highest point on mountain.

(2) Hartmann plates:  
 1 - three 2.25" apertures  
 2 - same as 1 with one hole blocked  
 3 - six 1.0" apertures

(3) Each data run (except exposure seg.) consists of ≈ 120 frames of data. Exposure time = 1/60 sec. for plates 1 and 2; 1/30 sec. for 3.

5. Effect of Hartmann aperture spacing.
6. Temporal variation in seeing.

#### D. Data Processing.

Initial data reduction was carried out using the David Mann Optical Comparator. This is a device which uses precision lead screws to position cross hairs on the desired location. Readout is automatic on IBM cards and a typewriter. Experienced operators working with well defined circular images (diameter  $\sim 10 \mu\text{m}$ ) quote measurements with a repeatability of less than three microns.

In order to determine the repeatability on our data, ten 2.25 inch Hartmann frames taken on August 23 (Run 8-1) were selected at random and read by two different operators. The procedure used was to visually estimate the center of one image and zero the readout. The center of a second image was then visually estimated and a reading recorded (displacement in two orthogonal directions). This procedure was repeated ten times on each frame by each operator.

The resulting data was first reduced for linear spacing. Averaged (smoothed) spacings and ten reading variances were then calculated for each frame. Finally, the ten frame averages and variances (of the smoothed values) were calculated. The results of this analysis are given in Table 6. As can be seen, the two sets of smoothed values are within one sigma (larger value) in

TABLE 6. SAMPLE DATA REDUCTION

	Separation ( $\mu\text{m}$ )		Standard Deviation ( $\mu\text{m}$ )	
	Operator 1	Operator 2	Operator 1	Operator 2
Single Frame No.				
1	348	349	1.9	6.5
2	358	355	4.3	4.4
3	336	331	6.1	3.4
4	335	350	6.2	3.4
5	353	354	4.1	5.4
6	294	298	3.7	5.6
7	375	380	3.7	7.2
8	334	328	4.7	6.4
9	333	326	3.8	6.0
10	318	317	3.3	4.0
Ten Frame Average	338.3	338.8	22.3	22.1



all cases except frame nine which has a slightly larger difference. Assuming the measurements are independent with Gaussian random read errors, the estimated sigma (due to read errors) associated with the ten frame averaged spacing should be of order 0.5  $\mu\text{m}$ . The estimated sigma associated with the ten frame root variance should be of order 0.4 and 0.8  $\mu\text{m}$  for the two operators, respectively. It should be noted that this analysis does not deal exactly with the quantization error ( $\pm 1 \mu\text{m}$ ) in the readout. However, the turbulence induced variances are expected to be larger than 1  $\mu\text{m}$  (as indicated in Table 6) and so this effect should not be significant.

A second check on errors was obtained by processing the same twenty-six frame data set on two different days (same operator). Five independent readings of each frame were made. The average spacings were 203.0  $\mu\text{m}$  and 204.8  $\mu\text{m}$  respectively. The standard deviations were 18.4  $\mu\text{m}$  and 17.6  $\mu\text{m}$ , respectively. These values are consistent with the errors indicated by the data of Table 6.

Based on these results, it appears that this technique should result in an accurate data reduction. The number of repeated readings on a single frame has been set at five. When combined with other parameters (number of frames processed  $\approx 100$ , expected levels of variances, etc.), we expect that a  $\pm 10\%$  measurement of the turbulence induced variation in spacing should be obtained.

## E. Results.

In all twenty data sets were reduced. The results, given in Table 7, are for seven nights over a span of nine days.

The image pair reduced had a 4.75 inch nominal aperture plane spacing,  $(V_1 - V_2)$ . As can be seen, these sets consist of three subsets in which data were collected inside and outside the observatory within a short period ( $\leq 45$  minutes). Preliminary estimates of the errors indicate that the first five cases are accurate to better than  $\pm 10\%$  (i.e., "standard deviation" of the standard deviation). However for data set 17-2, an excessive amount of defocus was used leading to large, under-exposed images that were more difficult to read. Therefore, errors may be somewhat higher than  $\pm 10\%$  for this case.

The values of  $(\Delta/f)$  were calculated from Eq. (A.4) using the measured mean values. Due to the smallness of this factor in all cases, its effect was ignored when calculating the angle of arrival via Eq. (A.5). A value of 224 inch was used for the focal length. The correlation scale,  $r_0$ , was calculated from Eqs. (A.7-A.9) assuming a coefficient of one half in Eq. (A.9) and a wavelength of  $0.5 \mu\text{m}$ . In addition, it was assumed that no correlation existed between the two apertures. The theoretical model of Fried<sup>11</sup> yields approximately the same results.

As can be seen, only one subset (15-1 and 15-2) of data indicates a major difference in angle of arrival variance inside

TABLE 7. DIFFERENTIAL ANGLE OF ARRIVAL MEASUREMENTS

Run	Date; Time	Location; $\theta_{EL}^{\circ}$	N	$\bar{r}$ ( $\mu\text{m}$ )	$\bar{v}^{1/2}$ ( $\mu\text{m}$ )	$(\Delta/R) \times 10^{-3}$	$\langle (\alpha - \alpha_1)^2 \rangle^{1/2}$ ( $\mu\text{rad}$ )	Derived $r_0$ (cm)	Corrected $r_0$ (cm)
B-1	8/22; 2340	Outside; 50	10	338	21	2.8	3.7	8.5	10.0
13-1	8/24; 2200	Outside; 67	49	442	26	3.7	4.5	6.8	7.2
13-2	8/24; 2300	Outside; 75	50	311	30	2.6	5.2	5.7	5.8
13-3	8/24; 2330	Outside; 68	50	297	21	2.5	3.7	8.5	8.9
13-4	8/25; 0015	Outside; 58	50	263	24	2.2	4.3	7.2	7.9
15-1	8/25; 2145	Outside; 65	72	372	33	3.1	5.8	5.0	5.3
15-2	8/25; 2230	Inside; 58	99	331	52	2.7	9.1	2.6	2.9
16-1	8/26; 0000	Inside; 55	79	270	41	2.2	7.2	3.8	4.3
16-2	8/26; 0030	Outside; 48	98	524	46	4.3	8.1	3.3	3.9
17-1	8/26; 2045	Inside; 60	79	210	22	1.7	3.9	8.1	8.8
17-2	8/26; 2130	Outside; 54	89	1192	28	4.4	4.9	6.1	6.9
19-1	8/27; 2100	Outside; 72	50	348	21	2.9	3.7	8.5	8.8
19-2	8/27; 2130	Inside; 68	49	309	18	2.6	3.2	10.3	10.8
20-1	8/29; 2030	Inside; 72	50	160	11	1.3	2.0	17.8	18.3
20-2	8/29; 2130	Inside; 68	50	140	12	1.2	2.1	16.7	17.5
20-3	8/29; 2200	Inside; 78	50	109	12	0.9	2.1	16.7	16.9
20-4	8/29; 2215	Inside; 75	50	89	13	0.7	2.3	15.2	15.5
21-1	8/30; 2045	Red Hill; 72	50	350	15	2.9	2.7	12.6	13.0
21-2	8/30; 2130	Red Hill; 68	50	378	14	3.1	2.5	13.9	14.5
21-3	8/30; 2245	Inside; 78	50	192	12	1.6	2.1	16.7	16.9

and outside the observatory. Based on the estimated 10% variance in the measurement of the sample variance ( $\sigma_r$ ), the difference represents roughly a four sigma change. The other two subsets have differences which are less than approximately one sigma and therefore cannot be considered statistically significant.

A rather surprising result is the small calculated values of  $r_0$ . Seeing is thought to be typically 1 arc sec which corresponds to an  $r_0$  of approximately 11 cm. The data taken on the night of August 25 implies seeing angles as large as 4 arc sec. Such values are not unreasonable, particularly in view of the fact that on the next night (8/26) the values of  $r_0$  were much closer to 11 cm. As the experiment continued, values of  $r_0$  increased, and this emphasizes the fact that this recording period may not be representative of year-round conditions at AMOS. Note also that microthermal and sounder measurements had ceased on 26 August, just before the seeing improved. All of the derived  $r_0$  values are plotted in Fig. 21 to further demonstrate the non-stationarity of this parameter.

All data were collected on stars well away from zenith. Theory<sup>12</sup> predicts a  $(\sin \theta_{EL})^{3/5}$  dependence for  $r_0$  leading to smaller values at large zenith angles. For example, making this correction to case 17-1 yields an  $r_0$  of 8.8 cm which corresponds approximately to vertical seeing angle ( $\sim \lambda/r_0$ ) of 1.2 arc sec. We have provided values of  $r_0$  corrected by this zenith angle

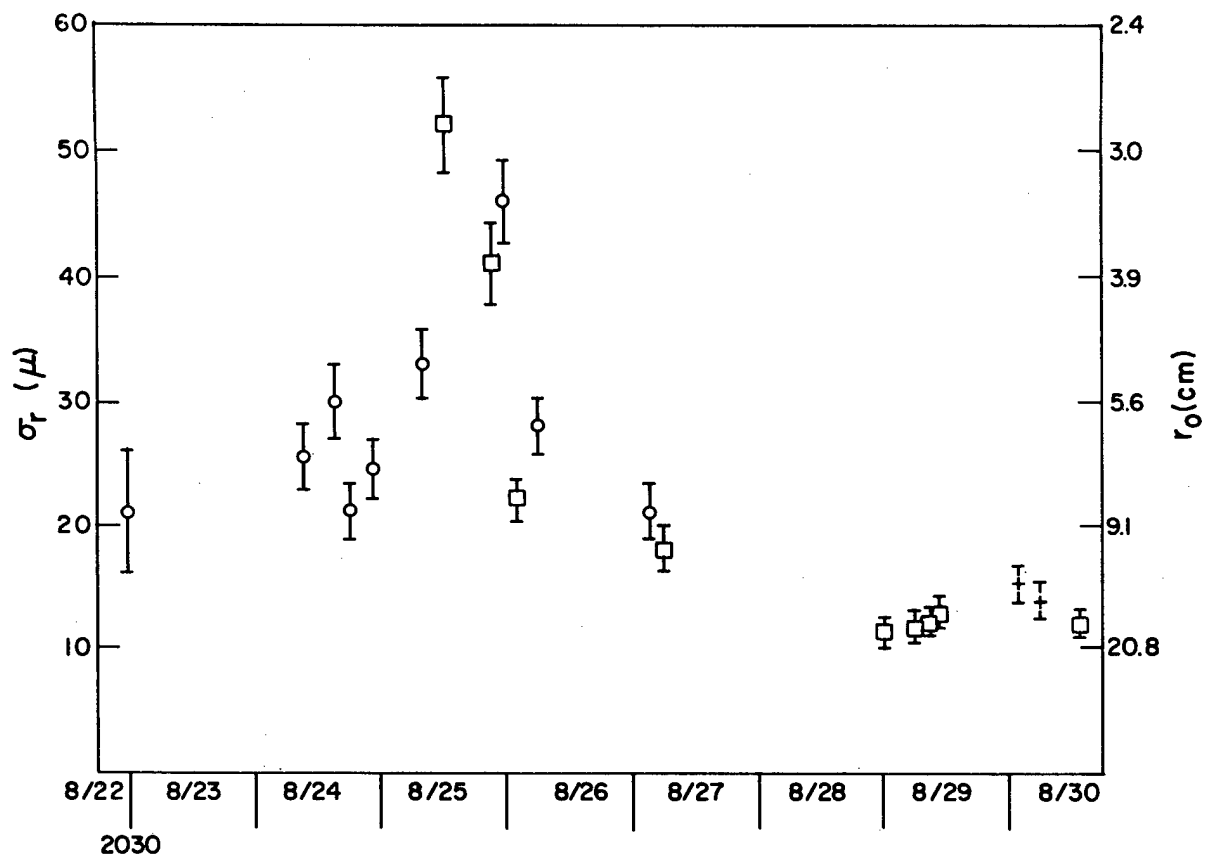


Figure 21. Measured Differential Angle of Arrival Standard Deviations and Derived Values of  $r_0$ . Locations of data collection are: O, outside observatory;  $\square$ , inside observatory; +, atop Red Hill. The bars indicated the estimated one  $\sigma$  spread in the data due to finite sample size.

dependence in Table 7 as a further reference. Now the values of  $r_0$  range from 2.9 to 18.3 cm with a mean of 10.2 cm.

## V. CONCLUSIONS

### A. Comparison of All Data

Within each of the previous sections we concluded with a table of  $r_0$  values for the runs in which good data were collected. Now we will compare those values for the times when all three experiments were in operation, and will include the two runs where only acoustic sounder data are missing. Furthermore we shall consider the percentage contribution of the regions sensed by the acoustic and fine-wire probes to the total turbulence as sensed by the Hartmann device.

Consider Table 8. The microthermal sensors gave us values of  $r_0$  ranging from 0.21 to 0.70 m in these runs. Although we used sensor 1, which was positioned well away from the dome and 4 m above ground, the values change little if we used sensor 4, on top the tower displaced 3 m from the dome, or sensor 6, mounted just outside the dome slot. Basically these sensors contribute a noticeable but small percentage to the overall. We may just say that these values of  $r_0$  can in the worst cases be a degrading influence on overall seeing. Recall that in Table 3, where we surveyed all the runs, some  $r_0$  were as low as 0.11 m. Thus on occasion the turbulence in the vicinity of the dome is a limiting factor. The important fact which we cannot derive conclusively from these data is whether the turbulence is actually coming from the buildings. Only during Runs

TABLE 8  
COMPARISON OF VALUES OF  $r_o$  (m) AND PERCENT CONTRIBUTION  
TO THE TOTAL  $r_o$  FOR ALL INSTRUMENTS  
WHEN ALL INSTRUMENTS WERE OPERATING SIMULTANEOUSLY

RUN	SENSOR 1 $r_o$ , %	ACOUSTIC $r_o$ , %	OPTICAL $r_o$ (100%)	MISSING %
8-1	0.21 , 29	missing	0.10	71
13-1	0.33 , 8	1.29 , 1	0.072	91
13-2	0.33 , 6	1.29 , 1/2	0.058	93.5
13-3	0.33 , 11	1.29 , 1	0.089	88
13-4	0.33 , 9	1.29 , 1	0.079	90
15-1	0.70 , 1	missing	0.053	99
15-2	0.70 , 1/2	missing	0.029	99.5
16-1	0.49 , 2	0.50 , 2	0.043	96
16-2	0.49 , 2	0.50 , 1	0.039	97
17-1*	0.24 , 19	0.95 , 2	0.088	79
17-2*	0.24 , 13	0.95 , 1	0.069	86

\*Used average of Runs 17 and 18 for sensor 1, as optical measurements were made between these runs.



15 and 16 does it appear that ambient turbulence is low (Sensors 1 and 3), but turbulence sensed by Sensors 4, 5 and 6 is quite strong.

The acoustic sounder data are more clear-cut. Values of  $r_0$  for the region of 100 to 1000 ft above the site are much too large to be a limiting factor, or even a contributing one.

The Hartmann device, in principle, should have indicated an improvement in seeing when it was moved from inside to outside the dome. That occurred only in one case, Runs 15-1 and 15-2, but in Runs 19-1 and 19-2 conditions *improved* by moving inside. Furthermore, the other runs showed no noticeable improvement or degradation incurred by moving the instrument outside. This further suggests that turbulence in the vicinity of the dome may be roughly a 10-30% contribution and hardly a constant in time.

According to Table 8, there is from 71 to 99.5% of the turbulence which was not sensed by the sounder or the fine-wire probes. This turbulence must be in the regions of 60 to 100 ft and above 1000 ft. We are inclined to think that the unaccounted turbulence is well above 1000 ft and may be associated with strong temperature inversions, such as at the tropopause.

The situation is slightly different at the 48" dome than at the 60" dome. Consistently we noted as much or more turbulence inside as outside the 48" dome; whereas the reverse was

true at the 60" dome. This would suggest a thermal contamination problem in the 48" dome, caused perhaps by heat exchangers, power supplies, etc. Either these might be removed or the heat so generated be vented downwind of the dome.

B. Summary of Conclusions.

We have tabulated all our conclusions with respect to seeing degradation and its causes at AMOS in the following list for convenience.

(1) The region of 100 to 1000 ft altitude does not have significant strengths of turbulence to degrade seeing.

(2) The turbulence in the vicinity of the dome structures can on occasion be a significant factor, but typically is only a 10-30% contribution to total seeing degradation.

(3) Local turbulence appears to be naturally generated in most instances, although in certain runs significant turbulence appeared to peel from the dome structures.

(4) Additional seeing degradation is caused by turbulence generated within the 48" dome when it is in roughly an operational configuration. The same would probably be true for the 60" dome were it operational.

(5) Significant turbulence must lie between 60 and 100 ft and above 1000 ft altitude, and may be centralized at temperature inversions such as the tropopause.

C. Recommendations and Future Work.

Any scheme which would reduce heat absorption on the outer surfaces would improve seeing a noticeable amount. This might include special paint, and venting and cooling of the outer wall. The inner walls stay cool and thus air conditioning is not required. The heat-generating equipment in the 48" dome should either be cooled in place or should be moved. This equipment will still generate heat no matter where it is, and one should be careful in positioning heat exchangers and vent ducts. The dome doors should be pointed away from the sun in the afternoon. This will not improve seeing when looking downwind but may improve it looking upwind.

A routine micrometeorological station is being set up at AMOS to do the measurements we discussed, excluding the Hartmann Test, continuously. The system involves two towers, one north and one south of the domes. On each tower will be three fine-wire sensors and a wind set (speed and direction). Also a thermometer will provide a continuous record of temperature. The acoustic sounder will be permanently installed as well. All the signals will be processed in real time by an on-site mini-computer which will identify the quality of seeing and will tell the operator when a sensor is not working properly. This system will ultimately satisfy a major objection to the August 1974 experiment, that it was of too short duration.

A series of ancillary experiments will be conducted

during 1975-76 which will provide further information on the seeing at AMOS. This includes two instruments which measure the atmospheric Optical Transfer Function (OTF) and thus  $r_0$  directly: the Hughes Research Lab Seeing Monitor (SM) and the ITEK Real Time Atmospheric Measurements System (RTAM). These instruments will be run simultaneously with the Hartmann device to mutually verify their outputs. An additional instrument being procured from NOAA measures the scintillation covariance function and provides a crude profile of turbulence. This will demonstrate whether the turbulence which appears to be at high altitudes really is at those heights. Other experiments to be run include rawinsonde launches from the top of Mt. Haleakala (to get a better picture of the wind and temperature in the immediate vicinity of the site) and aircraft flights with fine-wire probes (to measure  $C_T^2$  versus altitude for the first 7000 ft above AMOS).

Data from all of these measurements will then be combined to form a phenomenological turbulence model of AMOS. The objective is to provide data for the design of a compensated imaging system and data on seeing quality for routine site operation. Without a doubt this is the most intensive set of measurements ever performed on an observatory with the sole purpose of quantifying and improving seeing conditions.

## APPENDIX A

### THEORY RELATING HARTMANN TESTING TO SEEING VALUES

Consider a wave propagating from a distant point source, through the atmosphere to the image plane of a telescope. The image plane intensity is given by

$$I_I(\tilde{x}) \sim \left| \int d\tilde{v} W(\tilde{v}) A(\tilde{v}) \exp \left\{ \frac{-ik}{R} \tilde{x} \cdot \tilde{v} + i\phi_A(\tilde{v}) \right\} \right|^2, \quad (A.1)$$

where  $W(\tilde{v})$  is the aperture pupil function (assumed real) and  $A(\tilde{v})$  and  $\phi(\tilde{v})$  are the aperture plane amplitude and phase distortion generated by the atmosphere. The symbol  $k$  is the wave number, and  $R$  is the focal length of the telescope. Provided the telescope aperture ( $D$ ) is small with respect to the characteristic scale of the phase fluctuations ( $\Lambda_\phi$ ),  $\phi_A(\tilde{v})$  can be approximated by the first two terms in a Taylor series expansion yielding

$$I_I(\tilde{x}) \sim \left| \int d\tilde{v} W(\tilde{v}) A(\tilde{v}) \exp \left\{ -ik \left[ \frac{\tilde{x}}{R} - \left( \frac{\tilde{v} \phi_A(o)}{k} \right) \right] \cdot \tilde{v} \right\} \right|^2, \quad (A.2)$$

where  $\tilde{v} \phi_A(o)$  is the spatial derivative of the atmospheric phase evaluated at the center of the aperture. Equation (A.2) indicated that the image plane intensity is just a distorted Airy pattern (due to  $A$ ) with center at

$$\tilde{x}_C = \frac{R}{k} \tilde{v} \phi_A(o) \approx \tilde{\alpha} R \quad (A.3)$$

where  $\tilde{\alpha}$  is the angle of arrival, i.e., the angle between the

true and apparent direction of the star (as judged by the center of the image). Thus by observing the motion of the image of a star through a telescope of small aperture, these data can be reduced for the atmospheric angle of arrival fluctuations.

However, there is at least one difficulty with tracking the motion of a single star image. The position of the image also depends on telescope tracking and wind loading which cannot be separated from turbulence effects. Assuming that these two effects cause motion of the telescope as a whole, a convenient way of separating turbulence and tracking effects is to use two stars and reduce for the differential motion between the two images.

This same objective can be achieved with a single star by use of a telescope fitted with an aperture mask with two or more holes. By defocusing the image, a Fresnel image of the mask will be formed. This technique is basically a classical Hartmann test except that instead of processing a single frame of data, a series of short exposure images is processed for the required statistical information.

Modifying the above analysis to the case of a two hole Hartmann plate leads to a time averaged image position difference of

$$\langle x_1 - x_2 \rangle = (\Delta/f) (V_1 - V_2), \quad (A.4)$$

where  $f$  is the telescope focal length,  $\Delta$  is the amount of defocus

and  $(V_1 - V_2)$  is the separation of the Hartmann hole centers. The variance in the differential angle of arrival (one dimensional) is

$$\langle (\alpha_1 - \alpha_2)^2 \rangle = \frac{\langle (x_1 - x_2)^2 \rangle - \langle x_1 - x_2 \rangle^2}{f^2 (1 - \Delta/f)^2} . \quad (\text{A.5})$$

Equation (A.5) shows that provided  $(\Delta/f)$  is small, the amount of defocus used is not critical for a measurement of the angle of arrival variance. However it is important for establishing sensor requirements since it affects the energy density of the Hartmann images. The angular difference is related to the single aperture angle of arrival of Eq. (A.3) by

$$\langle (\alpha_1 - \alpha_2)^2 \rangle = \langle \alpha^2 \rangle C_{12} , \quad (\text{A.6})$$

where  $C_{12}$  accounts for any correlation between the two Hartmann apertures. Theoretical values of  $C_{12}$  have recently been calculated by Fried.<sup>11</sup>

Angle of arrival measurements can also fulfill the requirement of allowing extrapolation to large diameter apertures. For a small aperture instrument, it can be shown that<sup>12</sup> the squared variance of the angle of arrival (one component) is given by

$$\langle \alpha^2 \rangle = \frac{D_\phi(d)}{k^2 d^2} , \quad (\text{A.7})$$

where  $d$  is the aperture diameter and  $D_\phi$  is the phase structure function defined by  $\langle (\phi(x) - \phi(x+d))^2 \rangle$ . The long exposure

optical transfer function for an aperture of arbitrary size is given by<sup>13</sup>

$$\langle \tau(f) \rangle = \tau_0(\lambda Rf) e^{-\frac{1}{2}} [D_\ell(\lambda Rf) + D_\phi(\lambda Rf)], \quad (\text{A.8})$$

where  $D_\ell$  is the atmospheric log-amplitude structure function and  $\tau_0(\lambda Rf)$  is the lens (no atmosphere) MTF. It is usually this quantity that is used to specify classical resolution.

Assuming a Kolmogorov turbulence spectrum and the Rytov approximation,<sup>13</sup>

$$D(\rho) = D_\ell(\rho) + D_\phi(\rho) = 6.88(\rho/r_0)^{5/3} \begin{cases} 1/2 & \text{for } \rho \ll \sqrt{\lambda L} \\ 1 & \text{for } \rho \gg \sqrt{\lambda L} \end{cases}, \quad (\text{A.9})$$

provided  $\rho$  is larger than some small number (of order one millimeter or smaller). The symbol  $L$  is the pathlength through turbulence. Provided the model assumed is correct, the parameter  $r_0$  controls the shape of the long exposure MTF and hence classical resolution and seeing. From Eqs. (A.7) and (A.9) it can be seen that the angle of arrival variance can be used to determine  $r_0$ , at least to within a factor of  $2^{-3/5}$ . Thus from a measurement of  $\langle \alpha^2 \rangle$ , a minimum value of  $r_0$ , and hence a minimum resolution for a large aperture instrument can be implied.



## REFERENCES

- <sup>1</sup>R. Zirkind, *Appl. Opt.* 4, 1077 (1965).
- <sup>2,3</sup>(These references will be made available to qualified military or government request from RADC(OCSE), Griffiss AFB NY 13441.
- <sup>4</sup>D. P. Greenwood and D. O. Tarazano, *A Proposed Form for the Atmospheric Microtemperature Spatial Spectrum in the Input Range*, RADC-TR-74-19, Griffiss AFB NY (1974). (AD776 294)
- <sup>5</sup>D. P. Greenwood and D. B. Youmans, *A Fine-Wire Microtemperature Probe for Atmospheric Turbulence Measurements*, RADC Technical Report, Griffiss AFB NY (1975). (RADC-TR-75-240)
- <sup>6</sup>F. F. Hall, Jr., *Temperature and Wind Structure Studies by Acoustic Echo Sounding*, Ch 18 in *Remote Sensing of the Troposphere*, ed. by V. E. Derr (US Govt Printing Office #0323-0011, 1972).
- <sup>7</sup>D. A. Haugen, J. C. Kaimal and J. T. Newman, *The Use of an Acoustic Echo Sounder for Optical Tracking Application*, AFCRL Technical Report, Hanscom AFB MA (1975).
- <sup>8</sup>J. C. Kaimal, D. A. Haugen and J. T. Newman, *J. Appl. Meteorol.* 5, 411 (1966).
- <sup>9</sup>W. D. Neff, *Quantitative Evaluation of Acoustic Echoes from the Planetary Boundary Layer*, NOAA Tech Report ERL 322-WPL-38, Boulder CO (1975).
- <sup>10</sup>D. L. Fried, *Rad. Sci.* 10, 71 (1975).
- <sup>11</sup>D. L. Fried, *Theoretical Study of Non-Standard Imaging Concepts*, RADC-TR-74-185 (May 1974). (AD783 276)
- <sup>12</sup>R. S. Lawrence and J. W. Strohbehn, *Proc. IEEE* 58, 1523 (1970).
- <sup>13</sup>D. L. Fried, *J. Opt. Soc. Am.* 56, 1372 (1966).

# *MISSION of Rome Air Development Center*

RADC is the principal AFSC organization charged with planning and executing the USAF exploratory and advanced development programs for information sciences, intelligence, command, control and communications technology, products and services oriented to the needs of the USAF. Primary RADC mission areas are communications, electromagnetic guidance and control, surveillance of ground and aerospace objects, intelligence data collection and handling, information system technology, and electronic reliability, maintainability and compatibility. RADC has mission responsibility as assigned by AFSC for demonstration and acquisition of selected subsystems and systems in the intelligence, mapping, charting, command, control and communications areas.



Printed by  
United States Air Force  
Hanscom AFB, Mass. 01731